Nanoscale Advances

ROYAL SOCIETY OF CHEMISTRY

PAPER

View Article Online
View Journal | View Issue

Cite this: *Nanoscale Adv.*, 2026, **8**, 2426

Nitrogen-doped carbon quantum dots as fluorescent sensor for doxorubicin and chlortetracycline: experimental and DFT insights

Sondos Lotfy, [a] Mohamed M. Aboelnga, [ab] Elhossein A. Moawed [a] and Elsayed Elbayoumy *[a]

The accurate and rapid detection of clinically vital but potentially toxic pharmaceutical residues, such as the anticancer agent Doxorubicin (DOX) and the broad-spectrum antibiotic Chlortetracycline (CTC), is essential for therapeutic drug monitoring and environmental safety. This work presents the development of a novel fluorescent sensor based on nitrogen-doped carbon quantum dots (NEDA-CQDs) synthesized *via* a simple hydrothermal method using *N*-(1-naphthyl) ethylenediamine (NEDA) and citric acid (CA) as precursors. The obtained CQDs exhibited excellent aqueous dispersibility, strong blue fluorescence with a quantum yield (QY) of 2.7%, and high photostability. Comprehensive characterization revealed uniform quasi-spherical nanoparticles enriched with amino (NH_2), hydroxyl (OH), and carboxyl (COOH) functionalities. The NEDA-CQDs exhibited remarkable fluorescence quenching in the presence of DOX and CTC, allowing for their quantitative detection with limits of detection (LOD) of 4.02 μM and 2.53 μM, respectively. Stern–Volmer analysis demonstrated highly linear quenching behavior, indicating a combined static quenching and inner filter effect (IFE) mechanism. Application to human serum and urine samples resulted in excellent recoveries ranging from 93.65% to 106.34%, highlighting the practical utility of the sensor. Density functional theory (DFT) calculations further elucidated the sensing mechanism, demonstrating strong binding energies, significant HOMO–LUMO gap reductions, Fermi level shifts, and enriched non-covalent interactions (NCI), including π–π stacking and hydrogen bonding. Reduced density gradient (RDG) and NCI analyses confirmed the formation of a stable drug–sensor complex, consistent with the experimentally observed fluorescence quenching. Overall, the synergy between experimental findings and theoretical insights establishes NEDA-CQDs as an efficient, low-cost, and robust fluorescent nano-sensor for monitoring DOX and CTC in biological and environmental matrices.

Received 9th January 2026
Accepted 9th March 2026

DOI: 10.1039/d6na00019c

rsc.li/nanoscale-advances

1. Introduction

Antibiotics are a broad class of organic compounds with potent activity against pathogenic microorganisms and are extensively employed in human healthcare,[1] veterinary medicine,[2] agriculture,[3] and aquaculture.[4] However, their widespread and often indiscriminate application has led to growing concerns.[5] Residual antibiotics originating from animal production systems and environmental sources can be transferred to humans through the food chain, where they interfere with normal metabolic pathways, disrupt the gut microbiota, and pose direct risks to human health.[6] Furthermore, excessive and uncontrolled use accelerates the development of antimicrobial resistance genes,[7] a phenomenon that diminishes therapeutic efficacy and imposes long-term ecological and public health challenges. Among these, DOX, a widely used chemotherapeutic antibiotic, and CTC, a broad-spectrum tetracycline antibiotic, have received particular attention due to their extensive use and associated environmental and health impacts. Therefore, the development of efficient strategies for their sensitive detection and monitoring is of great significance to ensure both environmental safety and public health protection.

DOX is an anthracycline-based chemotherapeutic agent extensively employed in the treatment of various malignancies, including breast cancer, lymphomas, hematological cancers, and lung tumors.[8–11] Despite its remarkable therapeutic efficacy, fluctuations or excessive accumulation of DOX in biological fluids may trigger severe side effects such as nausea, alopecia, hepatotoxicity, vomiting, abdominal pain, and cardiotoxicity, thereby limiting its clinical applicability.[12–14] Accordingly, precise and real-time monitoring of DOX concentration is essential to balance therapeutic outcomes while minimizing adverse effects.

Similarly, CTC, a broad-spectrum tetracycline antibiotic consisting of four linearly fused tetracyclic rings, has been

[a]*Chemistry Department, Faculty of Science, Damietta University, New Damietta, Damietta, 34517, Egypt. E-mail: sayedelbayoumy@du.edu.eg*
[b]*Petroleum Chemistry Program, Faculty of Science, King Salman International University, Ras Sudr, South Sinai, 46612, Egypt*

widely applied not only for the treatment of human infections but also in animal husbandry for preventing intestinal diseases and promoting growth.[15,16] Nevertheless, its widespread and often uncontrolled usage has led to significant health and environmental concerns. Residual CTC has been detected in food products such as milk, meat, and honey, where it poses risks to human health by inducing allergic reactions, gastrointestinal disturbances, and hepatotoxicity.[17–20] Furthermore, environmental accumulation of CTC residues contributes to ecological contamination and accelerates the proliferation of antibiotic-resistant bacteria.[21–23]

Taken together, the potential toxicity of DOX and CTC, along with their persistence in biological and environmental systems, highlights the urgent need for sensitive, selective, and reliable detection strategies. Developing advanced sensing platforms for these antibiotics is therefore of great significance for ensuring patient safety, food quality, environmental protection, and effective antimicrobial management. A wide range of analytical techniques has been established for monitoring DOX and CTC, reflecting the growing demand for precise and reliable detection. Commonly employed methods include high-performance liquid chromatography (HPLC),[24–26] electrochemical methods,[27–29] mass spectrometry,[30] chemiluminescence,[31,32] capillary electrochromatography,[33] and immunoassays.[34–36] While these techniques are recognized for their high sensitivity and specificity, they suffer from several drawbacks, including costly instrumentation, labor-intensive sample preparation, time-consuming analysis, and the need for skilled personnel. Moreover, their applicability in routine or on-site testing is limited. These challenges have motivated increasing research into alternative sensing platforms that are rapid, cost-effective, and capable of delivering high selectivity and sensitivity in complex biological and environmental matrices.

Among the various analytical techniques, fluorescence spectroscopy has emerged as a powerful tool owing to its simplicity, high sensitivity, and rapid response compared with conventional methods.[37–39] Despite these advantages, the development of fluorescent sensors that simultaneously meet the criteria of low cost, ease of synthesis, high stability, and strong selectivity for DOX and CTC detection remains a considerable challenge.[40–46] Fluorescence-based sensing has gained considerable attention for the detection of both DOX and CTC owing to its simplicity, high sensitivity, and rapid response compared with conventional methods.[47] For DOX, diverse nanomaterials such as graphene quantum dots,[48,49] metal-based quantum dots,[50,51] molecularly imprinted polymers,[52,53] and metal nanoclusters[54–56] have been employed, achieving low detection limits with excellent recovery in biological fluids. For instance, carbon dot-based sensors demonstrated strong π–π interactions with DOX and enabled fluorescence quenching-based assays,[57–61] while upconversion nanoparticles[62–64] and gold nanocluster[65] probes provided ultrasensitive detection and high selectivity in real samples.

Similarly, numerous fluorescence strategies have been reported for CTC detection, including citrate-modified g-C_3N_4 nanodots with aggregation-induced emission enhancement,[66] gold[67,68] and copper nanoclusters,[69,70] and a range of MOF-based probes[71–73] that achieved sub-micromolar to nanomolar detection limits. Smartphone-assisted platforms coupled with ratiometric and AI-supported fluorescence analysis have further advanced CTC sensing,[74,75] enabling portable and on-site monitoring. Collectively, these studies highlight the versatility and practicality of fluorescence-based methods for monitoring DOX and CTC residues in biological and environmental matrices, underscoring their promise for clinical and food safety applications.[76–82]

Fluorescent carbon quantum dots (CQDs), typically less than 10 nm in size, have emerged as a novel class of nanomaterials that have attracted significant research interest due to their distinctive optical and electrochemical properties.[83] Compared with conventional organic fluorescent dyes, CQDs offer several advantages, including excellent photostability, high chemical and biological compatibility, robust inertness, and low toxicity, which make them highly suitable for applications in bioanalysis and bioimaging.[84,85] Furthermore, their surfaces can be readily functionalized with hydrophilic groups such as ethylenediamine, polyethylene glycol (PEG), and polyethyleneimine (PEI) to extend their versatility in sensing applications.[86,87] To date, CQDs have been successfully employed in detecting molecular analytes, metal ions, and pH values across various systems.[88–93]

Recently, biomass-derived and heteroatom-doped CQDs have been widely explored for pharmaceutical sensing and bioimaging applications. For example, CQDs synthesized from renewable biomass precursors have demonstrated quantum yields ranging from 12–48% and detection limits in the low micromolar to nanomolar range for antibiotics and anticancer drugs.[94,95] Similarly, advanced surface-passivated CQDs exhibited enhanced selectivity windows and improved fluorescence efficiency through surface-engineering and heteroatom-doping strategies.[96,97] While these systems demonstrate high sensitivity, many rely on complex biomass sources, multi-step purification, or lack theoretical insight into the binding mechanism.

In parallel with experimental progress, density functional theory (DFT) has been increasingly applied to study the molecular-level interactions of DOX and CTC with nanostructured materials,[98–105] offering valuable insights into adsorption and sensing mechanisms.[106–108] Despite these advances in both experimental fluorescence sensing and computational studies, current strategies still face limitations such as costly or complex probe fabrication, restricted selectivity in multi-analyte systems, and insufficient integration of theoretical predictions with practical sensing applications. Therefore, there remains a pressing need to design low-cost, stable, and highly selective CQD-based fluorescence sensors, supported by DFT insights, for the effective detection of antibiotics such as DOX and CTC in biological and environmental samples.

In contrast to many previously reported biomass-derived systems, the present study employs a rationally designed precursor strategy combining citric acid and *N*-(1-naphthyl) ethylenediamine (NEDA), where the extended aromatic framework of NEDA introduces enhanced π–π stacking capability

together with nitrogen-rich surface functionalities. This structural design promotes strong interactions with aromatic drug molecules such as DOX and CTC while maintaining a simple, cost-effective, and reproducible hydrothermal synthesis route.

The main objective of this work is therefore to develop a highly efficient nitrogen-doped carbon quantum dots (NEDA-CQDs) fluorescent sensor for the sensitive detection of DOX and CTC in biological matrices. To accomplish this, NEDA-CQDs were synthesized and comprehensively characterized using TEM, XRD, FT-IR, XPS, and detailed optical analyses to elucidate their morphology, structural features, surface chemistry, fluorescence behavior, stability, and quantum yield. Their sensing performance was systematically evaluated through Stern–Volmer analysis and spectral overlap investigations to clarify the quenching mechanism. Importantly, unlike many previous reports, the sensing mechanism is further supported by extensive DFT calculations, including binding energy determination, HOMO–LUMO gap analysis, Fermi level shifts, RDG, and NCI mapping, providing molecular-level insight into drug–sensor interactions. The integration of experimental validation and theoretical modeling establishes NEDA-CQDs as a robust and mechanistically well-supported fluorescent nano-sensor for real-sample monitoring of DOX and CTC.

2. Experimental section

2.1. Materials and reagents

All reagents and chemicals used in this study were of analytical grade and employed as received without further purification. Distilled water (H_2O) was used throughout the experiments. Citric acid monohydrate ($C_6H_8O_7 \cdot H_2O$), hydrochloric acid (HCl), sodium hydroxide (NaOH), and ethanol (C_2H_5OH) were purchased from Fisher Scientific (Pittsburgh, Pennsylvania, USA). *N*-(1-Naphthyl) ethylenediamine dihydrochloride (NEDA·2HCl), doxorubicin hydrochloride ($C_{27}H_{29}NO_{11} \cdot HCl$), chlortetracycline hydrochloride ($C_{22}H_{23}ClN_2O_8 \cdot HCl$), coumarin 334 (C334), glucose, uric acid, triglycerides, theophylline, digoxin, and amino acids were obtained from Sigma-Aldrich (Merck, Darmstadt, Germany). The amino acids used included tryptophan (Trp), methionine (Met), alanine (Ala), glutamic acid (Glu), DL-proline (Pro), lysine (Lys), cysteine (Cys), and DL-aspartic acid (Asp).

2.2. Instruments

Spectroscopic analyses were carried out using a range of instruments. UV-vis absorption spectra were recorded on a Jasco V-630 spectrophotometer with a 1.0 × 1.0 cm quartz cuvette, within the wavelength range of 200–800 nm. Fluorescence measurements were performed on a Jasco FP-8350 spectrofluorometer equipped with a 150 W xenon lamp and a 1.0 cm quartz cuvette. The excitation wavelength was fixed at 405 nm, and emission spectra were collected over 440–650 nm with both excitation and emission band widths set to 5 nm. The pH values of the solutions were adjusted using a Jenway 3510 digital pH meter. FTIR spectra were obtained with a Jasco FTIR-4100 spectrophotometer in the range of 4000–500 cm^{-1}, using KBr discs. Transmission electron microscopy (TEM) images were obtained using Model Talos L120C G2–TEM–ThermoFisher–Europe. Dynamic light scattering (DLS) and Zeta potential analysis were performed using a Malvern Zetasizer Nano-ZS90 (Malvern, UK) at 25 °C with a conductivity of 0.0133 mS cm^{-1}. The powder X-ray diffraction (XRD) patterns were recorded on a Siemens D-500 diffractometer using Cu-Kα radiation (λ = 0.15406 nm), scanned at a rate of 10° min^{-1} over a 2θ range of 3°–80°. X-ray photoelectron spectroscopy (XPS) analysis was performed using an Omicron XPS spectrometer equipped with a Mg Kα radiation source (1254 eV) to examine the chemical composition and binding energies of the NEDA-CQDs.

2.3. Solution preparation

Stock solutions of amino acids and theophylline were prepared individually at a concentration of 1.0 × 10^{-3} mol L^{-1} by dissolving the required amounts of each compound in deionized water. A coumarin 334 solution (1.0 × 10^{-3} mol L^{-1}) was prepared by dissolving 2.83 mg of the compound in 10.0 mL of ethanol.[109]

2.4. Synthesis of NEDA-CQDs

NEDA-CQDs were synthesized *via* a one-step hydrothermal method using citric acid (CA) and *N*-(1-naphthyl) ethylenediamine (NEDA) as precursors according to the reported procedure illustrated in Scheme 1.[59,110] Briefly, 0.50 g of CA and 0.0125 g of NEDA were dissolved in 50 mL of distilled water under continuous stirring until a homogeneous solution was obtained. The resulting solution was transferred to a 50 mL Teflon-lined stainless-steel autoclave and heated at 160 °C for 8 h in a muffle furnace. After completion of the reaction, the autoclave was allowed to cool naturally to room temperature, yielding a yellowish-brown solution. To remove large particles and unreacted residues, the obtained solution was first centrifuged at 5000 rpm for 30 min. The supernatant was then filtered through a 0.22 μm syringe filter, followed by further purification using dialysis against deionized water to eliminate small molecular impurities and excess precursors. After dialysis, the purified, water-soluble NEDA-CQDs solution was collected and stored at 4 °C in a refrigerator. The prepared NEDA-CQDs remained stable for more than three months, with no noticeable change in their optical properties until further use.

2.5. Fluorescence detection of DOX, CTC, and interference studies

Fluorescence-based detection of DOX and CTC was carried out at room temperature employing NEDA-CQDs as the fluorescent probe. Sensitivity experiments were performed using a fluorescence titration method.[111–113] In a typical assay, 20 μL of the water-soluble NEDA-CQD solution was mixed with 2000 μL of distilled water, followed by the addition of 10–200 μL of DOX or CTC solutions at a concentration of 1000 μM. The mixtures were then analyzed using a fluorometer at an excitation wavelength of 405 nm, and the emission spectra were recorded over the range of 450–650 nm.

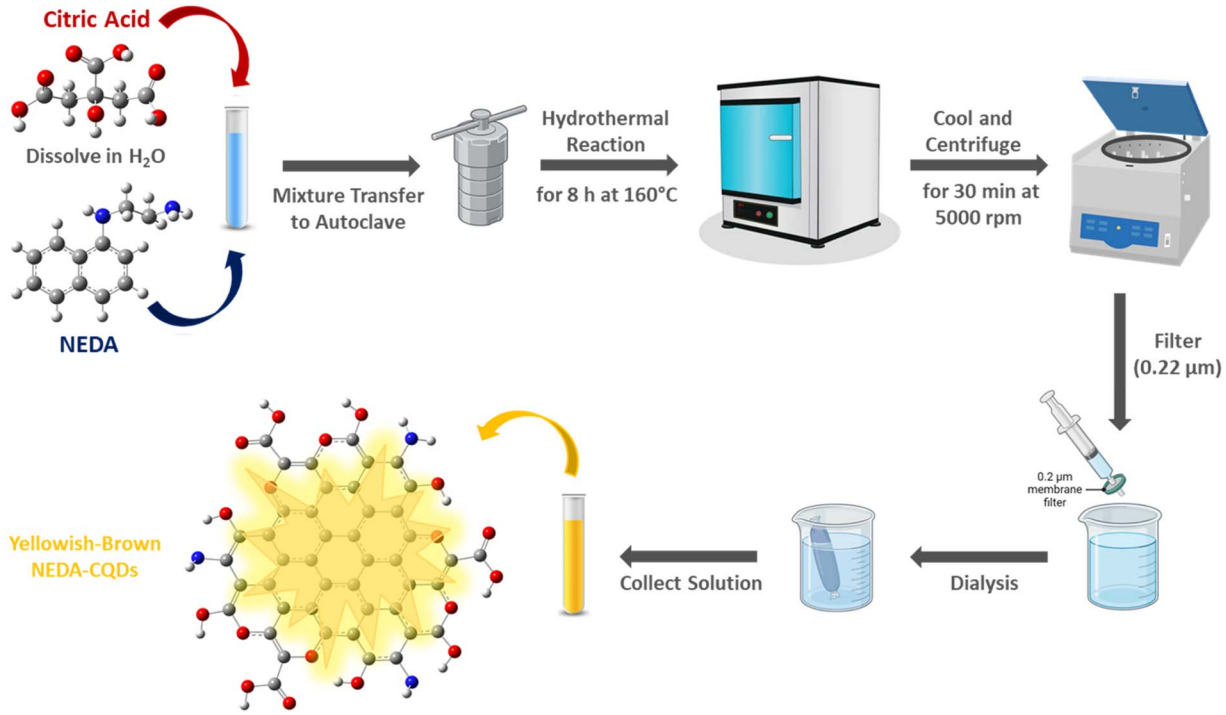

Scheme 1 Synthesis of the *N*-(1-naphthyl) ethylenediamine carbon quantum dots (NEDA-CQDs).

The fluorescence quenching efficiency was evaluated by comparing the relative fluorescence intensity (I/I_0) of NEDA-CQDs in the absence (I_0) and presence (I) of the drugs. Selectivity studies were performed under identical conditions by replacing the drug solutions with 500 μL of glucose, uric acid, triglycerides, theophylline, digoxin, or various amino acid solutions (1.0×10^{-3} mol L^{-1}) to assess potential interference effects. All measurements were conducted in triplicate to ensure reproducibility.

2.6. Detection of DOX and CTC drugs in biological samples

The applicability of NEDA-CQDs for detecting DOX and CTC drugs was evaluated using human plasma and urine samples obtained from a healthy adult volunteer who is the first author of the manuscript. The study involved no clinical intervention, diagnostic procedure, or therapeutic treatment, and the samples were used solely for analytical method validation. According to institutional regulations for non-clinical laboratory-based analytical studies involving voluntary self-sampling, formal ethical committee approval was not required.

Plasma samples were centrifuged at 3000 rpm for 15 min to separate serum, while urine samples were centrifuged at 4500 rpm for 20 min to remove suspended particles. The resulting supernatants were collected and stored in the refrigerator at 4 °C until use. Before analysis, each supernatant was diluted 100-fold with distilled water and spiked with known concentrations of DOX or CTC. Quantitative analysis of DOX and CTC in the spiked urine and serum samples was performed using the standard calibration curve method. The final concentrations were calculated as the mean of three replicate measurements, and recovery percentages were determined from the corresponding fluorescence intensity and absorbance values.

2.7. Computational methods

DFT analyses were carried out using the Gaussian 09 software package.[114] The hybrid B3LYP-D3 functional,[115–118] combined with the 6-31G(d,p) basis set, was employed to optimize the geometries of the NEDA-CQDs nanosheet, DOX, and CTC drug molecules and their corresponding complexes in the gas phase. This functional was chosen for its proven effectiveness and reliability in accurately describing the electronic properties of various molecular systems.[119–124] The optimized geometries, frontier molecular orbitals (HOMO–LUMO), and molecular electrostatic potential (MEP) maps were visualized using GaussView 6.0. The reduced density gradient (RDG) and non-covalent interaction (NCI) analyses were performed with Multiwfn[125] and visualized using VMD[126] and Gnuplot.[127] The density of states (DOS) spectra were generated using the GaussSum program.[128] The binding energy (E_{bind}) was calculated according to the following equation:

$$E_{bind} = E_{NEDA\text{-}CQDs/Drug\ Molecules} - (E_{NEDA\text{-}CQDs} + E_{Drug\ Molecules}) \quad (1)$$

Here, $E_{NEDA\text{-}CQDs}$ indicates the energy of the NEDA-CQDs nanosheet, $E_{Drug\ Molecules}$ represents the energy of the isolated drug molecules, and $E_{NEDA\text{-}CQDs/Drug\ Molecules}$ corresponds to the total energy of the complex formed after their interaction. The HOMO–LUMO energy gap (E_g) is determined as the difference

between the LUMO energy (E_{LUMO}) and the HOMO energy (E_{HOMO}),[129] and can be expressed as follows:

$$E_g = E_{LUMO} - E_{HOMO} \quad (2)$$

The change in E_g values, which is used to analyze the electronic properties of the systems, is represented by the following equation:

$$\Delta E_g\ (\%) = \left(\frac{E_{g2} - E_{g1}}{E_{g1}}\right) \times 100 \quad (3)$$

here, E_{g1} and E_{g2} refer to the energy gap values before and after the binding of the drug molecules, respectively. The percentage change in the energy gap ΔE_g (%) reflects the alteration in E_g upon drug binding on the sensor surface. The Fermi level energy (E_F) is calculated using the following equation:[130]

$$E_F = \left(\frac{E_{LUMO} + E_{HOMO}}{2}\right) \quad (4)$$

3. Results and discussions

3.1. Characterization of the NEDA-CQDs

3.1.1. TEM analysis. The TEM image of NEDA-CQDs reveals well-dispersed, quasi-spherical nanoparticles without noticeable aggregation, indicating good stability and uniform morphology, as shown in Fig. 1(A) and (B). The particle size distribution (Fig. 1(C)) exhibits a near-Gaussian profile with an average diameter of 5.79 nm and a standard deviation of ± 1.63 nm, indicating a relatively narrow size distribution and good uniformity of the prepared carbon quantum dots.

The observed particle size below 10 nm confirms the successful formation of carbon quantum dots, which is consistent with the typical size range reported for CQDs synthesized *via* hydrothermal methods. The small particle size and good dispersion are favorable for fluorescence properties and sensing performance due to the high surface-to-volume ratio and abundant surface functional groups.

Overall, the TEM analysis confirms that synthesized NEDA-CQDs are well-dispersed, nearly monodisperse, and suitable for fluorescence-based sensing applications.

3.1.2. DLS and zeta potential analysis. The particle size and colloidal stability of the synthesized NEDA-CQDs were further investigated using dynamic light scattering (DLS) analysis (Fig. 1(D)) and zeta potential measurement (see Fig. S1 in the SI). The DLS results showed a narrow volume-based size distribution with an average hydrodynamic diameter (8.11 ± 0.25 nm) larger than the TEM size, which can be attributed to the presence of a hydration layer and possible slight aggregation of carbon quantum dots in aqueous dispersion. Such behavior is commonly observed for carbon-based nanomaterials, where DLS measures the hydrodynamic size rather than the core particle size.

The zeta potential value of NEDA-CQDs was measured to be approximately −4.6 mV, indicating the presence of surface functional groups such as: (–OH, $–NH_2$, and –COOH) originating from the citric acid and *N*-(1-naphthyl) ethylenediamine precursors. These functional groups contribute to the surface charge and hydrophilicity of the NEDA-CQDs and help maintain their dispersion in aqueous media. Although the absolute zeta potential value is relatively low, the dispersion remained stable without visible precipitation for a long storage time, suggesting that steric stabilization in addition to electrostatic effects may contribute to the colloidal stability.

Overall, the good agreement between TEM, DLS, and zeta potential results confirms the successful synthesis of well-dispersed and stable NEDA-CQDs suitable for fluorescence sensing applications.

3.1.3. XRD analysis. The crystalline structure of NEDA-CQDs was investigated using XRD, and the corresponding diffraction pattern is presented in Fig. 2(A). The XRD spectrum exhibits multiple diffraction peaks located at 2θ values of 17.75°, 19.11°, 25.70°, 29.58°, 30.68°, 33.24°, 35.71°, 40.77°, and 42.77°, indicating the presence of crystalline domains within the carbon-based nanostructure.

The diffraction feature around $2\theta \approx 25°$ can be attributed to the (002) plane of graphitic carbon, suggesting the formation of partially ordered sp^2 carbon domains. The presence of additional diffraction peaks may be associated with nitrogen-containing surface functionalities and structural ordering induced by NEDA incorporation during the hydrothermal process.

These results indicate that the synthesized NEDA-CQDs possess a partially crystalline carbon framework with graphitic characteristics rather than a completely amorphous structure. The nanoscale crystallite domains embedded within the carbon matrix contribute to structural stability while maintaining the surface states responsible for fluorescence emission. A summary of the diffraction parameters, including 2θ, height, *d*-spacing, and relative intensity, is presented in Table S1 in the SI.

3.1.4. FT-IR analysis. The FT-IR spectrum of NEDA-CQDs is displayed in Fig. 2(B). The broad, intense absorption peaks observed at 3498.24 and 3294.79 cm^{-1} are attributed to O–H (hydroxyl) and/or N–H (amine) stretching vibrations, with the broad profile indicating hydrogen bonding interactions.[131] The distinct, sharp peak at 1715.37 cm^{-1} is assigned to C=O stretching of carboxylic acid functionalities.[132] A medium absorption at 1420.32 cm^{-1} is linked to in-plane bending vibration peaks of C–H or C–N bonds.[57,133] It is also possible that the band observed at 1420.32 cm^{-1} originates from the stretching vibrations of C=C bonds within aromatic rings. Strong absorptions in the 1214.93–1058.73 cm^{-1} range belong to C–O (carboxylic acid), C–N (amine), or C–O–C (ether) stretching vibrations, confirming the incorporation of multiple oxygen-containing groups on the CQD surface during synthesis.[110] Additionally, sharp bands at 940.128 and 882.274 cm^{-1} indicate out-of-plane C–H bending of aromatic rings or C–C skeletal vibrations. The sharp band at 774.279 cm^{-1} is associated with aromatic C–H bending, while the signals between 687.498 and 495.616 cm^{-1} represent out-of-plane deformations of aromatic rings.[134]

3.1.5. XPS analysis. The surface chemical composition of the synthesized NEDA-CQDs was analyzed using XPS. As shown

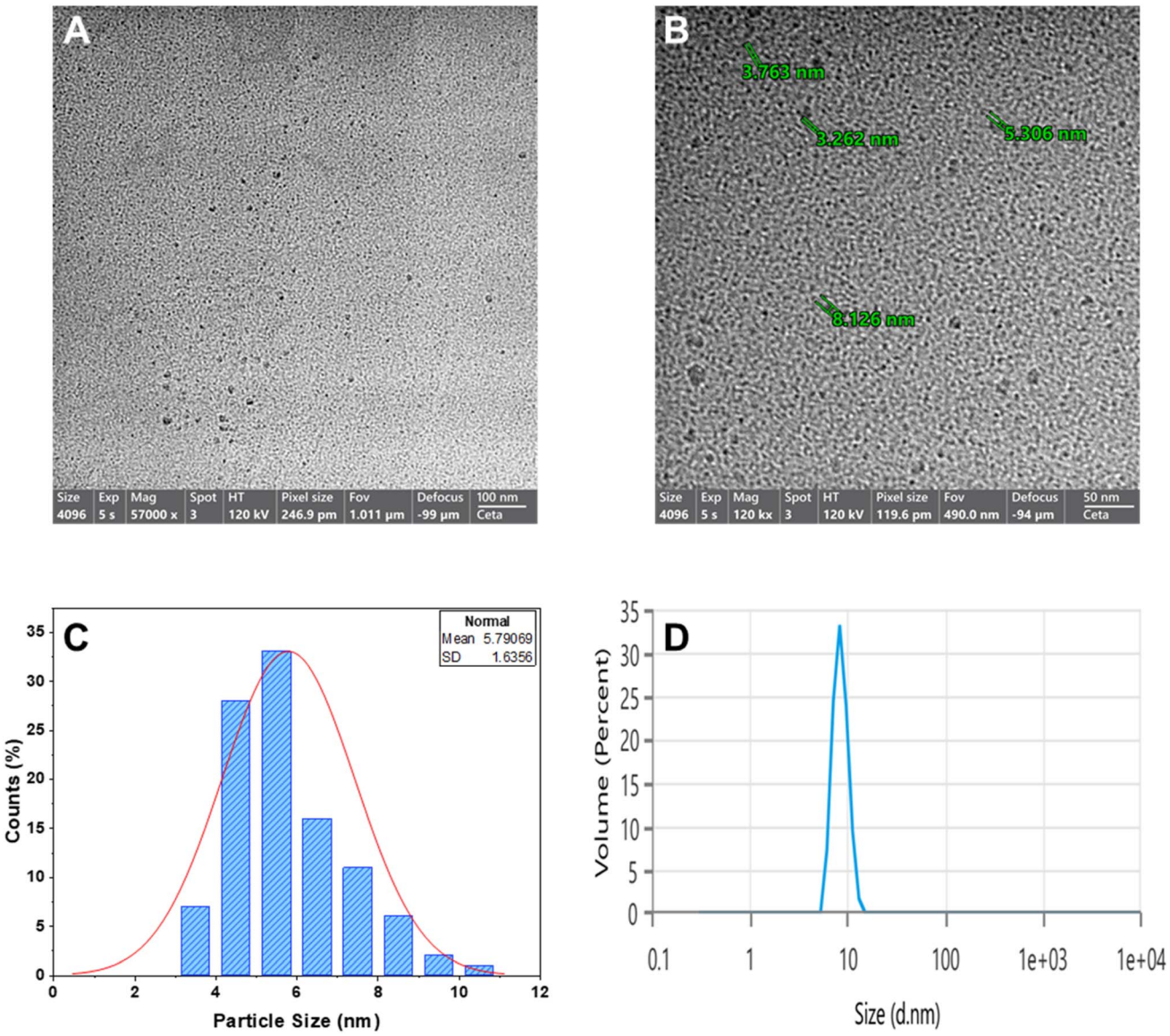

Fig. 1 (A and B) The TEM images, (C) particle size distribution analysis, and (D) DLS analysis for the NEDA-CQDs sensor, respectively.

in Fig. 2(C), the survey spectrum exhibits three distinct peaks at 286.83, 400.64, and 533.94 eV, corresponding to C 1s, N 1s, and O 1s, with atomic percentages of 68.36%, 4.2%, and 27.44%, respectively.[135] The high-resolution C 1s spectrum (Fig. 2(D)) displays components at 284.38 eV (C–C/C═C), 285.96 eV (C–N/C–O), and 287.61 eV (C═O/O–C═O), confirming the coexistence of sp^2 carbon, nitrogen, and oxygen functionalities.[136] The N 1s peaks at 398.38 and 399.54 eV correspond to C–N and N–H bonds (Fig. 2(E)),[137] while the O 1s peaks at 532.71 and 534.17 eV are assigned to C═O/O–C═O and C–OH/C–O–C groups (Fig. 2(F)).[138] These results indicate that oxygen and nitrogen are successfully incorporated into the CQD surface, and partial oxidation occurred during synthesis.

3.2. Optical properties of the NEDA-CQDs

The optical behavior of NEDA-CQDs was examined by UV-vis and fluorescence spectroscopy in distilled water over the wavelength range of 200–800 nm (Fig. 3(A)). The UV-vis spectrum displays two distinct absorption bands at 229 and 275.5 nm. The strong, sharp peak at 229 nm corresponds to π–π* transitions of double bonds (C═C) within the conjugated aromatic carbon core, while the broader band at 275.5 nm is attributed to n–π* transitions associated with lone pair electrons of oxygen and nitrogen functional groups introduced by the NEDA precursor.

The fluorescence emission spectrum (Fig. 3(B)) exhibits a strong emission peak centered at 492 nm under excitation at 405 nm, confirming the excellent photoluminescent properties of the synthesized NEDA-CQDs. Furthermore, emission spectra recorded at different excitation wavelengths (300–405 nm) revealed that the emission maximum remained nearly unchanged at ~490 nm, with only variations in intensity observed (see Fig. S2 in the SI). This behavior indicates predominantly excitation-independent fluorescence,

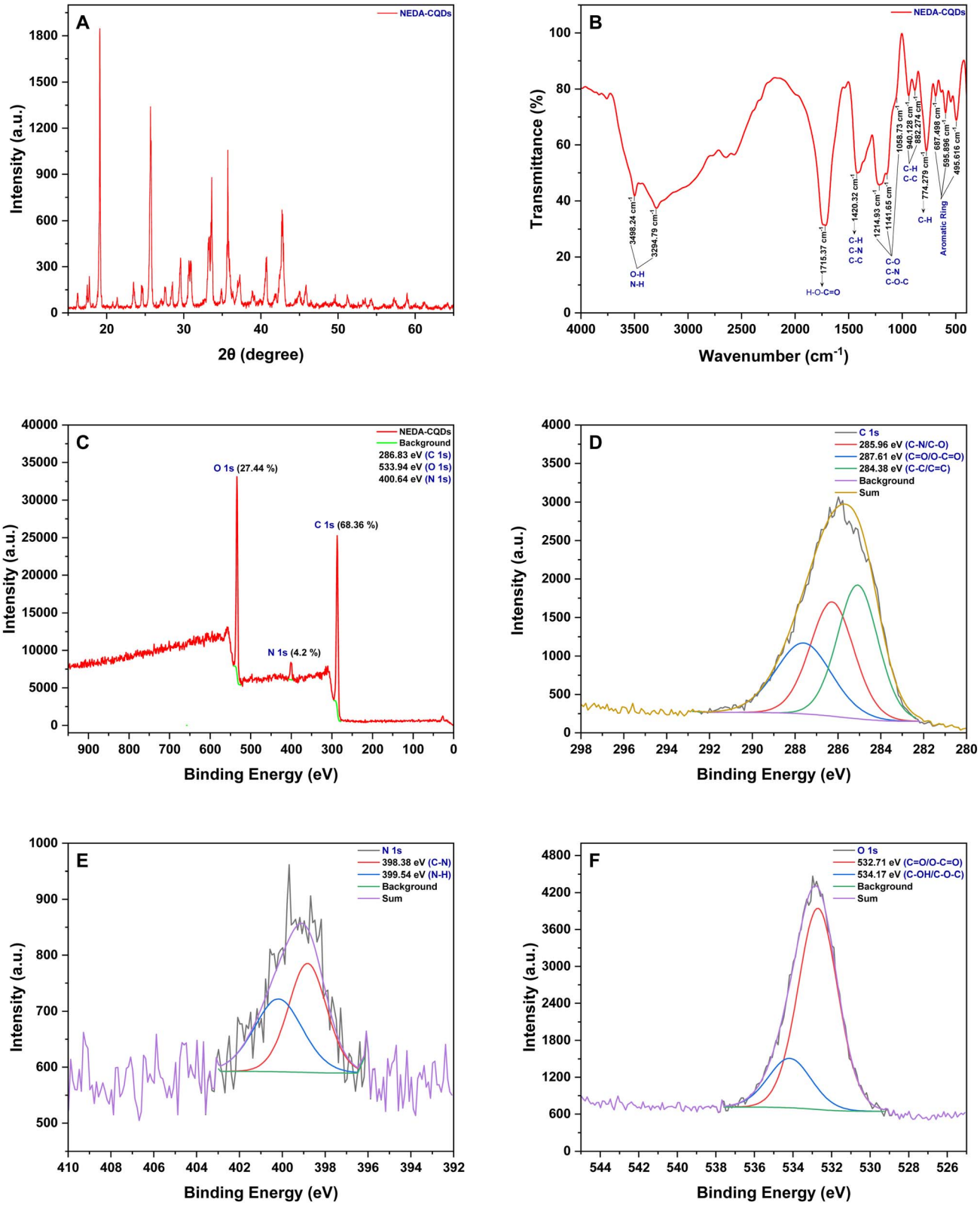

Fig. 2 (A) The XRD patterns, (B) FT-IR spectrum, (C) XPS full spectra, (D) C 1s spectrum, (E) N 1s spectrum, and (F) O 1s spectrum for the NEDA-CQDs sensor, respectively.

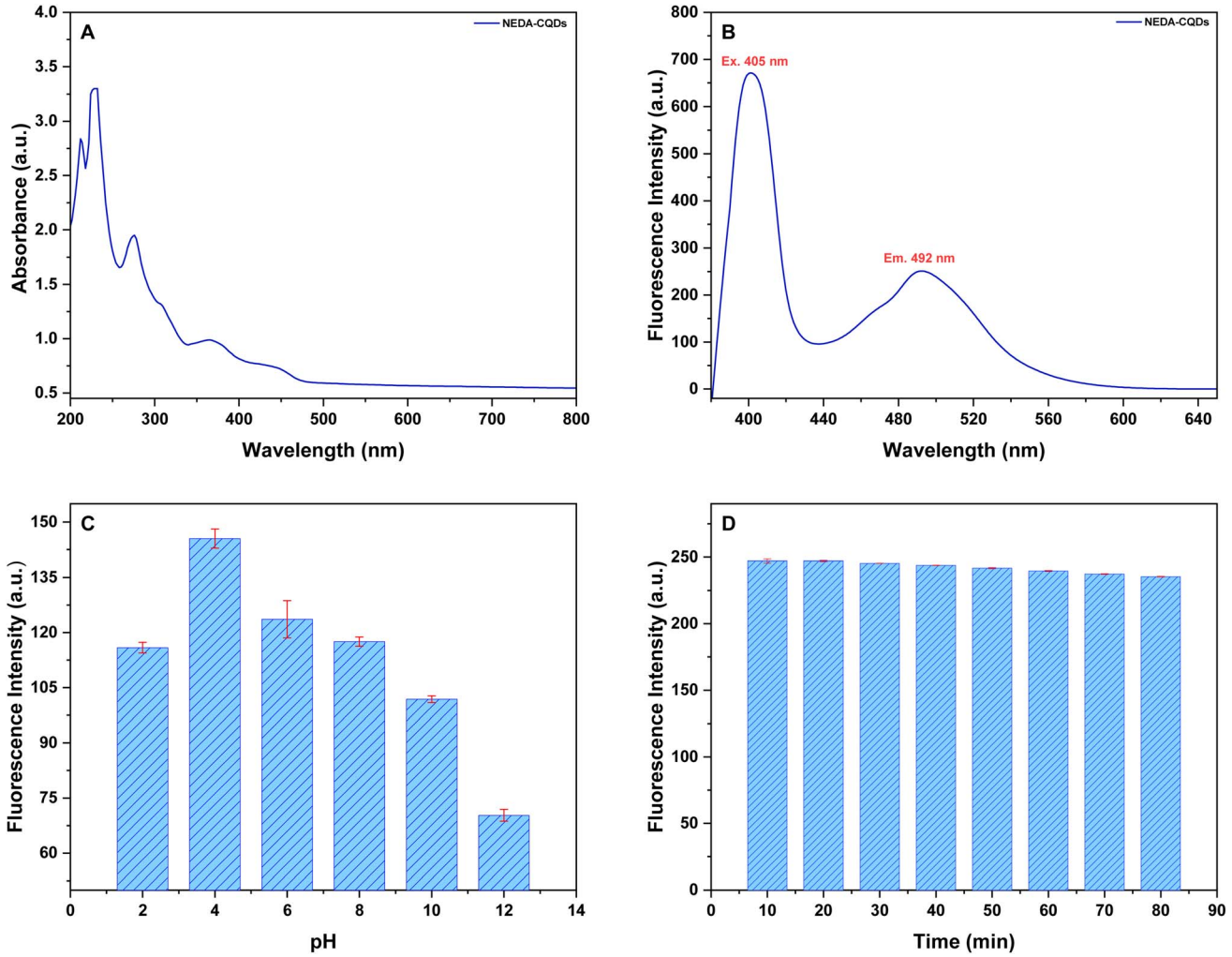

Fig. 3 (A) The UV-vis absorption spectra, (B) fluorescence emission spectra, (C) fluorescent intensity under different pH values, the pH was adjusted by adding concentrated HCl (0.1 M) or NaOH solution (0.1 M), and (D) fluorescent intensity under different times for the NEDA-CQDs sensor, respectively.

suggesting that the emission originates mainly from uniform surface emissive states rather than multiple trap states.

3.3. Fluorescence stability of NEDA-CQDs

3.3.1. Effect of pH. The influence of pH on the fluorescence behavior of NEDA-CQDs was examined in different pH solutions ranging from 2 to 12, as presented in Fig. 3(C). The fluorescence intensity increased notably between pH 2 and 4, then gradually decreased as the pH rose from 6 to 12. This variation is attributed to the reversible protonation and deprotonation of the amine and carboxyl groups on the NEDA-CQDs surface, which change the electronic structure of the fluorophore and act as an on/off switch for fluorescence in the acidic and basic media.[113,139] The more alkaline the solution, the more deprotonated the amine groups become, leading to a stronger quenching effect and a lower fluorescence intensity, as observed at pH 10 and 12. The highest emission observed at mildly acidic pH 4 and the gradual quenching toward basic media highlight the pH sensitivity and potential of NEDA-CQDs as reusable and responsive fluorescent pH sensors.

3.3.2. Effect of time. Fig. 3(D) illustrates the fluorescence intensity of the NEDA-CQDs sensor measured over a period of 80 minutes. The data demonstrate the sensor's excellent photostability under continuous measurement conditions. The fluorescence intensity of the NEDA-CQDs remains nearly constant throughout the entire duration, indicating that prolonged exposure to excitation light does not cause any noticeable photobleaching or degradation of the carbon quantum dots.

The observed stability can be attributed to the strong carbon core structure and effective surface passivation by NEDA functional groups, which protect the emission sites from oxidation and photochemical damage. This inherent robustness ensures consistent fluorescence emission without signal fluctuation or decay.

Moreover, no precipitation or floating particles were observed for over three months, further confirming the superior colloidal and fluorescence stability of the NEDA-CQDs. Such long-term dispersion stability and resistance to photodegradation make NEDA-CQDs a highly promising fluorescent

probe for reliable, real-time, and continuous sensing applications in environmental and biological systems.

3.4. Measurement of fluorescence quantum yield of NEDA-CQDs

The fluorescence quantum yield (QY) of NEDA-CQDs was determined using a relative comparative method according to the following equation:[140]

$$Q_s = Q_r\left(\frac{m_s}{m_r}\right)\left(\frac{n_s}{n_r}\right)^2 \quad (5)$$

where Q_s and Q_r are the quantum yields of the sample and reference, m_s and m_r are the slopes obtained from the linear fitting of integrated fluorescence intensity *versus* absorbance, and n_s and n_r are the refractive indices of the solvents used for the sample and reference, respectively. Coumarin 334 (C334) in ethanol ($n_r = 1.361$) was used as the reference standard with a reported quantum yield of 0.89. NEDA-CQDs were dispersed in distilled water ($n = 1.333$). The excitation wavelength was fixed at 405 nm for both the reference and the sample, and the emission spectra were recorded with the emission maximum located at approximately 492 nm for NEDA-CQDs.[109]

Integrated fluorescence intensity was plotted as a function of absorbance for Coumarin 334 and NEDA-CQDs, and the slopes were obtained from linear regression fitting (see Fig. S3 in the SI). The calculated slopes together with the refractive index correction were used to determine the quantum yield of NEDA-CQDs, which was found to be 0.027. All measurements were carried out at room temperature under identical instrumental conditions to ensure a reliable comparison between the reference and the sample.

3.5. Fluorescent detection of DOX and CTC drugs by the NEDA-CQDs sensor

The ability of NEDA-CQDs to detect DOX and CTC drugs was evaluated using a fluorescence titration method. The fluorescence response of the NEDA-CQDs sensor toward varying concentrations of DOX and CTC was systematically investigated, as illustrated in Fig. 4(A) and (C). Upon gradual addition of DOX or CTC, a gradual decrease in the fluorescence intensity of NEDA-CQDs was observed, indicating a clear fluorescence quenching effect. The fluorescence intensity of NEDA-CQDs decreased significantly as the concentration of DOX increased from 0 to 240 μM and CTC increased from 0 to 270 μM, respectively.

This significant fluorescence quenching behavior suggests a strong interaction between NEDA-CQDs and DOX or CTC molecules, indicating the involvement of an efficient electron or energy transfer mechanism and supporting their applicability in fluorescence-based sensing systems. To quantitatively evaluate the quenching process, the experimental data were analyzed using the Stern–Volmer equation:[141,142]

$$\frac{F_o}{F} = 1 + K_{SV}[M] \quad (6)$$

where F_o and F are the fluorescence intensities of NEDA-CQDs before and after the addition of DOX or CTC, respectively, K_{SV} is the Stern–Volmer quenching constant, and $[M]$ is the molar concentration of the quencher (DOX or CTC). The resulting Stern–Volmer plots (Fig. 4(B) and (D)) exhibited excellent linearity with correlation coefficients ($R^2 = 0.99$) for both DOX and CTC, confirming a direct and reliable relationship between fluorescence quenching and drug concentration. The linear regression equations were determined to be:

$$\text{NEDA-CQDs/DOX: } F_o/F = 1.04554 + 0.0039\ [\text{DOX}] \quad (7)$$

$$\text{NEDA-CQDs/CTC: } F_o/F = 1.02387 + 0.0024\ [\text{CTC}] \quad (8)$$

The strong linearity and high sensitivity of these calibration equations validate the suitability of NEDA-CQDs as an efficient fluorescent probe for quantitative drug detection in analytical applications. The calculated limit of detection (LOD) and limit of quantification (LOQ) were found to be 4.02 μM and 12.18 μM for DOX, and 2.53 μM and 6.67 μM for CTC, respectively.

These results highlight the superior analytical performance of the NEDA-CQDs sensor, exhibiting excellent sensitivity and a broad detection range for DOX and CTC. The strong fluorescence quenching response and high Stern–Volmer constants confirm the feasibility of using NEDA-CQDs as a robust and reliable fluorescent sensor for the sensitive detection of pharmaceutical compounds in biological samples.

3.6. Selectivity and anti-interference of the detection system

To evaluate the selectivity of the NEDA-CQDs toward DOX and CTC, interference studies were conducted using thirteen potentially competing biomolecules at a concentration of 1.0×10^{-3} M. The investigated species included tryptophan (Trp), methionine (Met), alanine (Ala), glutamic acid (Glu), DL-proline (Pro), lysine (Lys), cysteine (Cys), DL-aspartic acid (Asp), glucose, uric acid, triglycerides, theophylline, and digoxin. The fluorescence intensity of the NEDA-CQDs was recorded before and after the addition of each interferent, and the results are summarized in Fig. 5(A) and (B). As observed, all tested biomolecules induced only minor fluorescence changes, with quenching efficiencies ranging from 0.9% to 20% relative to the initial emission intensity of the NEDA-CQDs. In contrast, under identical experimental conditions, the addition of DOX and CTC resulted in significantly higher fluorescence quenching efficiencies of 76.8% and 78.1%, respectively. The pronounced difference in quenching response clearly demonstrates the preferential interaction of NEDA-CQDs with DOX and CTC over structurally unrelated biomolecules, confirming the high selectivity of the proposed sensor and supporting its suitability for reliable drug detection in complex biological environments.

3.7. Fluorescence quenching mechanism

The fluorescence sensing mechanism of CQD-based probes is generally governed by several possible pathways, including fluorescence resonance energy transfer (FRET), photoinduced electron transfer (PET), intramolecular charge transfer (ICT/

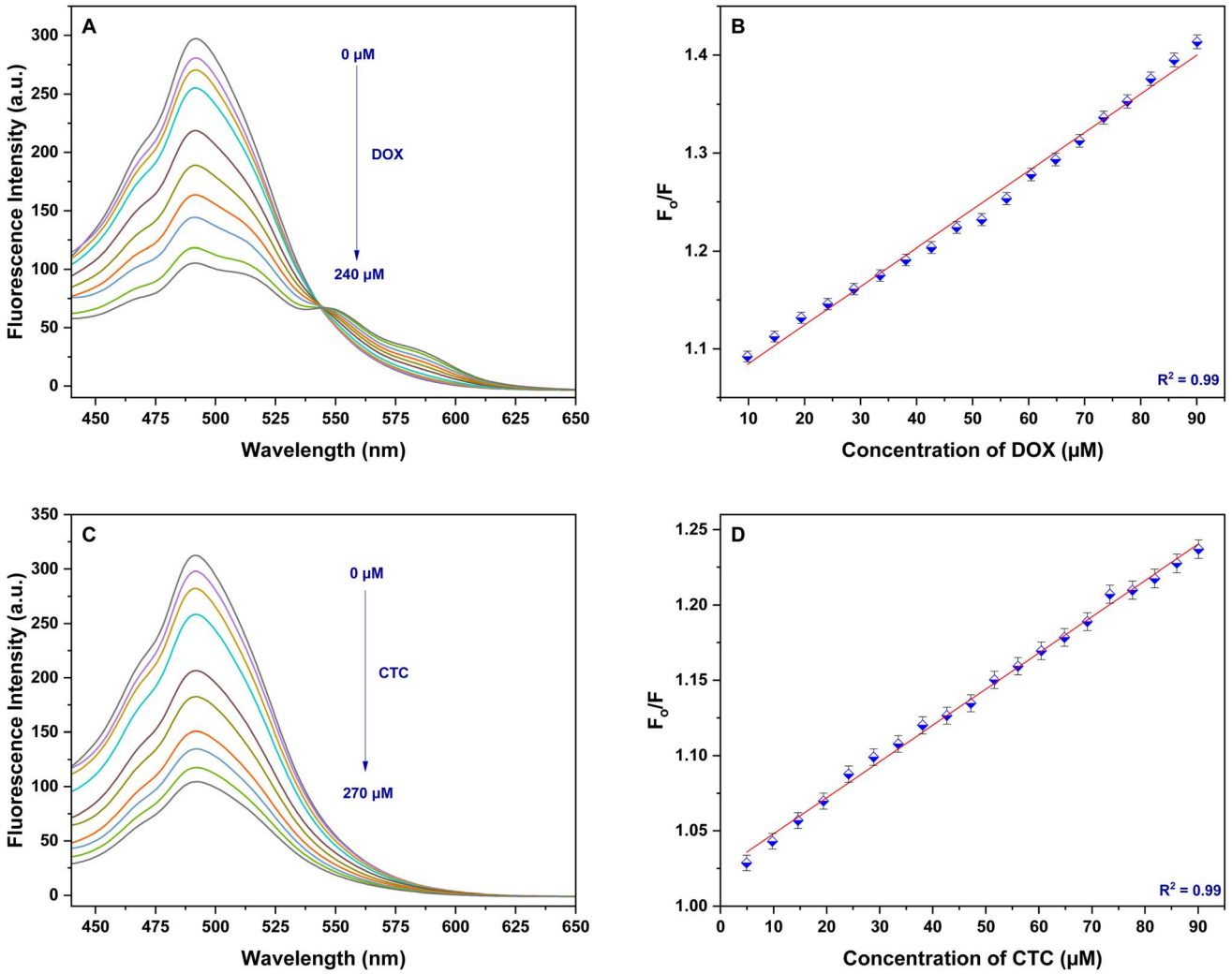

Fig. 4 The fluorescence emission spectra of the NEDA-CQDs sensor upon the addition of different concentrations of the (A) DOX and (C) CTC drugs in the ethanol solvent at room temperature. The Stern–Volmer linear plot of the F_0/F *versus* the concentration of the (B) DOX and (D) CTC drugs.

TICT), and inner filter effect (IFE).[143] Fluorescence quenching typically occurs through either dynamic or static processes. While dynamic quenching relies on collisional interactions between the fluorophore and the quencher in the excited state, static quenching involves the formation of a stable, non-fluorescent complex in the ground state between the fluorophore and quencher before excitation.

In the current system, the fluorescence quenching of NEDA-CQDs in the presence of DOX or CTC is primarily attributed to a combined inner filter effect (IFE) and static quenching mechanism.[52,57] The difference between static and dynamic quenching is identified through UV-vis absorption spectra. In a dynamic quenching process, the absorption spectrum of the fluorophore remains unchanged upon the addition of the quencher because the interaction only occurs during the lifetime of the excited state. However, as illustrated in Fig. 6(A) and (C), the addition of DOX or CTC to the NEDA-CQDs solution led to noticeable changes in the absorption profile of the sensor, indicating clear evidence for a static quenching mechanism.

Specifically, the characteristic absorption peaks of the NEDA-CQDs (represented by the dashed black line in Fig. 6(A) and (C)) exhibit a noticeable decrease and shift as the drug concentration increases. At the same time, new absorption peaks emerge in the visible region at 400–550 nm and 320–430 nm, corresponding to the DOX and CTC drug molecules, respectively. The disappearance of the original electronic transition peaks of the sensor, accompanied by the emergence of these new spectral bands, provides definitive evidence of a static quenching mechanism. This behavior indicates the formation of a stable, non-fluorescent ground-state complex between the NEDA-CQDs and the drug molecules, rather than simple transient collisions. Furthermore, these spectral alterations confirm significant modifications in the CQDs' electronic structure, likely arising from efficient charge or energy transfer processes within the newly formed complex.

The formation of the ground-state complex is attributed to multiple non-covalent interactions between the NEDA-CQDs surface and the functional groups of the DOX and CTC drug

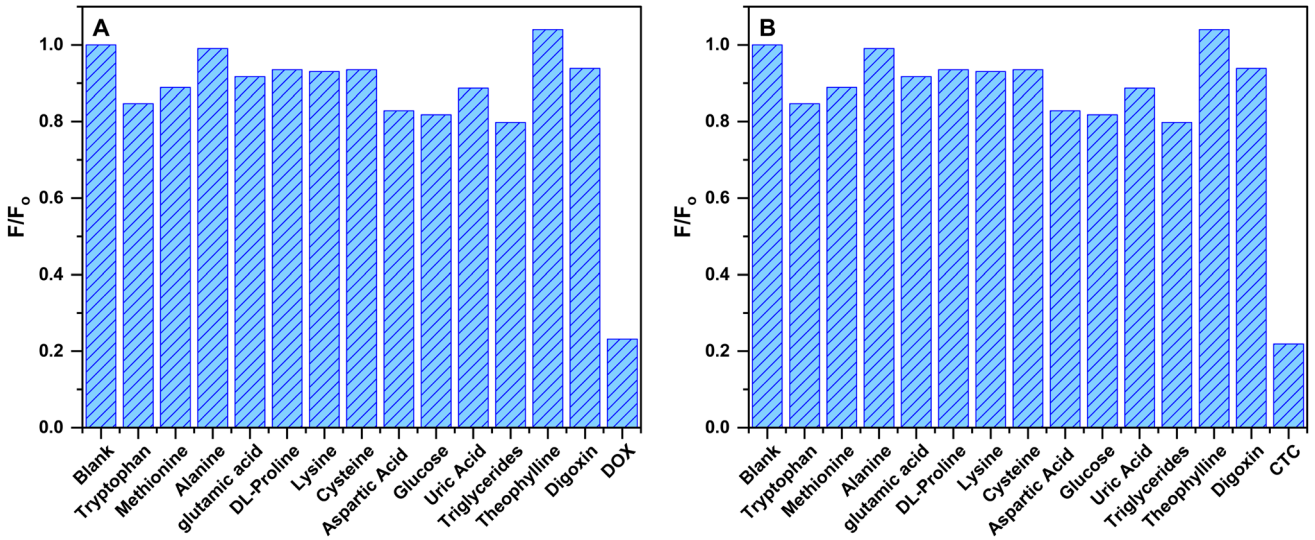

Fig. 5 Selectivity and anti-interference of the NEDA-CQDs sensor for (A) DOX and (B) CTC drugs over other biomolecules, respectively.

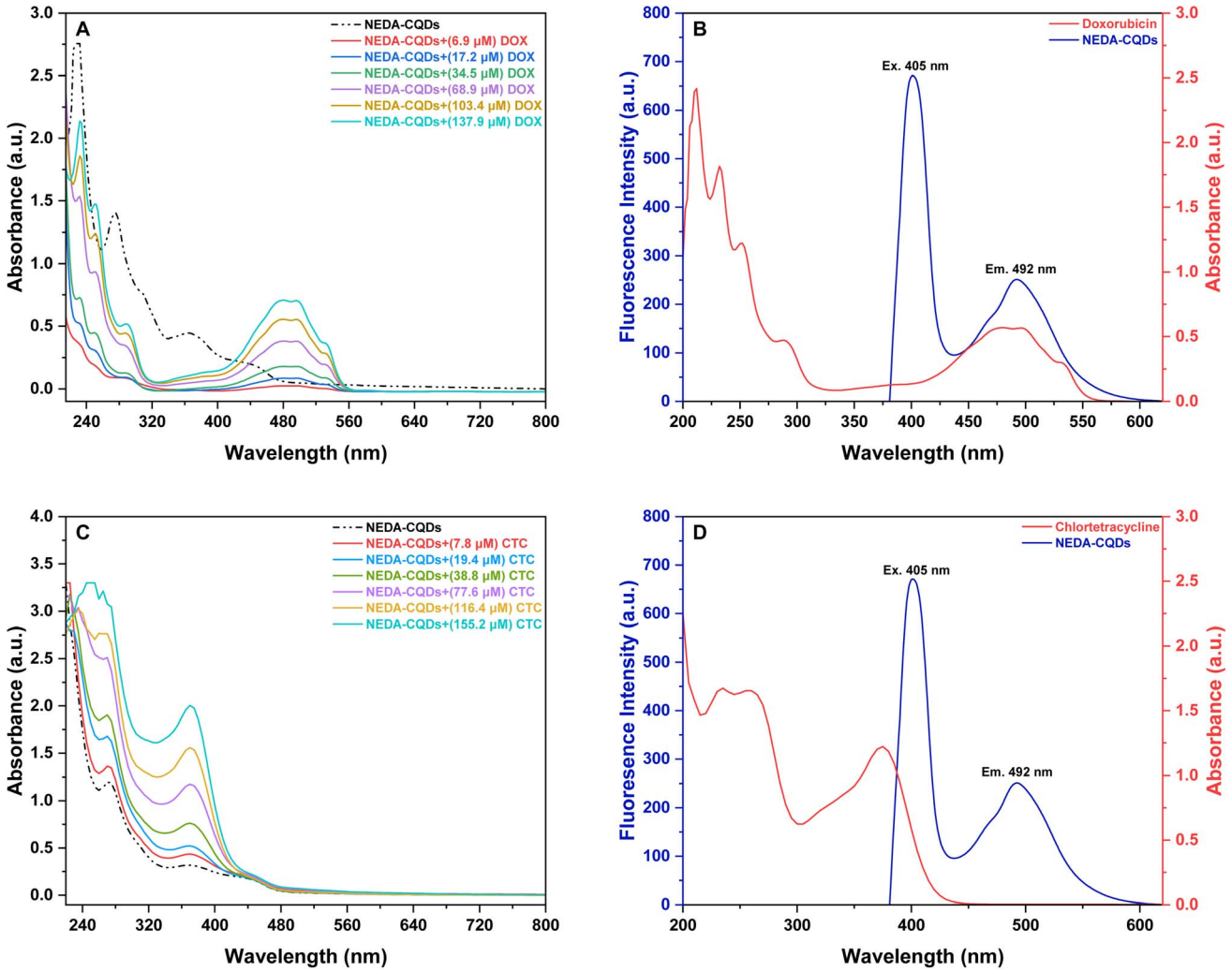

Fig. 6 The UV-vis absorption spectra of the NEDA-CQDs sensor before and after the addition of different concentrations of the (A) DOX and (C) CTC drugs. The spectral overlap between the UV-vis absorption curve of the (B) DOX and (D) CTC drugs and the fluorescence excitation and emission spectra of the NEDA-CQDs sensor.

Table 1 Determination of DOX and CTC drugs in human serum and urine samples using NEDA-CQDs sensor

Drugs	Samples	Concentration of drugs: Standard colorimetric method (μM) ± SD	Concentration of drugs: NEDA-CQDs sensor (μM) ± SD	Recovery (%)	RSD (%, $n = 3$)
DOX	Serum	21.996 ± 0.215	23.391 ± 0.228	106.339	0.97
	Urine	23.304 ± 0.075	21.824 ± 0.070	93.651	0.32
CTC	Serum	31.704 ± 0.046	32.988 ± 0.047	104.049	0.14
	Urine	30.454 ± 0.364	30.970 ± 0.370	101.694	1.19

molecules. The nature of these interactions may include π–π stacking interactions, hydrogen bonding, or electrostatic attractions. These interactions effectively disturb the surface states and radiative recombination pathways of the NEDA-CQDs, leading to a noticeable fluorescence quenching effect.

In addition to static quenching, the inner filter effect (IFE) plays a major role in the observed fluorescence quenching. As shown in the spectral overlap (Fig. 6(B) and (D)), the UV-vis absorption spectra of DOX and CTC drugs (red lines) significantly overlap with both the excitation ($\lambda_{ex} = 405$ nm) and the emission ($\lambda_{em} = 492$ nm) bands of the NEDA-CQDs sensor (blue lines). This overlap indicates that the drug molecules act as an "optical filter," absorbing the incident excitation light and reabsorbing the emitted photons from the NEDA-CQDs before reaching the detector. This evidence supports that the inner filter effect is a major contributor to the observed quenching mechanism in these systems.

In conclusion, the fluorescence quenching of NEDA-CQDs by DOX and CTC is governed by a synergetic mechanism combining static quenching driven by ground-state complexation and the inner filter effect (IFE). This robust interaction ensures the high sensitivity and reliability of the sensor for pharmaceutical detection.

3.8. Detection analysis of DOX and CTC drugs in real biological samples

To evaluate the practical applicability of the developed probe, NEDA-CQDs were employed as a fluorescent sensor for the detection of DOX and CTC drugs in biological samples. Known concentrations of each drug were spiked into diluted human urine and serum, and the analyte contents were quantified using the standard addition recovery method. As summarized in Table 1, the recoveries for DOX and CTC ranged from 93.561% to 106.339%, with relative standard deviations (RSDs) between 0.14% and 1.19% ($n = 3$). These results demonstrate that NEDA-CQDs possess excellent accuracy and precision, confirming their potential as an effective fluorescent platform for detecting trace amounts of DOX and CTC in biological fluids.

3.9. Analytical comparison of the NEDA-CQDs sensor with reported fluorescent sensors

To evaluate the analytical performance of the proposed NEDA-CQDs sensor, a comprehensive comparison with previously reported fluorescent sensing platforms for DOX and CTC detection is summarized in Table 2. The comparison includes key analytical parameters, including linear detection range, quantum yield, solvent system, sensing mechanism, and real-sample applications.

For DOX detection, several reported carbon dot-based systems exhibit relatively narrow linear ranges or require complex matrices and organic solvents. In contrast, the developed NEDA-CQDs sensor demonstrates a wide linear range (0–90 μM) in distilled water without the need for organic solvents or surface post-modification. Moreover, unlike many previously reported systems relying mainly on IFE or FRET mechanisms, our system exhibits dominant static quenching behavior supported by DFT calculations, providing deeper mechanistic insight into the sensing process.

For CTC detection, although some reported probes exhibit higher quantum yields, they often involve multicomponent nanocomposites, metal–organic frameworks, or rare-earth upconversion nanoparticles, which increase synthesis complexity and cost. The proposed NEDA-CQDs offer a simpler one-step hydrothermal synthesis using an *N*-rich aromatic precursor, enabling strong π–π stacking and electrostatic interactions with both analytes. Importantly, dual-analyte detection (DOX and CTC) is achieved using a single sensing platform, which is rarely reported.

These combined features demonstrate the practical applicability and competitive analytical performance of the developed sensor compared with previously reported fluorescent platforms.

3.10. Computational analysis

In developing the computational model of the proposed NEDA-CQDs nanosheet, the chemical structure was selected to match the experimentally determined surface chemistry. FT-IR characterization revealed the presence of hydroxyl (OH), amine (NH_2), carbonyl (C═O), carboxylate (COOH), and ether (C–O–C) functional groups (derived from NEDA), while XPS analysis confirmed carbon sp^2 domains along with C–N, C–O, C═O, and O═C–O bonding environments. These experimental results were used as the basis for constructing a representative CQD structure incorporating oxygen- and nitrogen-containing groups, which guided the functionalization of the polyaromatic hydrocarbon core in the computational model, ensuring that the DFT simulations accurately reflect the actual

Table 2 Comparison of the proposed NEDA-CQDs fluorescence sensor with previously reported fluorescent sensing platforms for the detection of DOX and CTC drugs

Fluorescence sensor	Linear range (μM)	Quantum yield (%)	Solvent	Sensing mechanism	Application	Ref.
DOX						
NEDA-CQDs	**0–90**	**2.7**	**Distilled water**	**Static quenching and IFE**	**Human serum and urine samples**	**Present work**
$Ru(dpp)_3$	Lower than 100	36.6	Acrylonitrile	—	Human urine samples	47
$CuInSe_2$@ZnS QDs/Ag NPs	2–100	16.51	Ultrapure water	Electrostatic interactions	Human serum samples	50
HCQDs@MIP	0.431–216	—	Ultrapure water	Static quenching and IFE	—	52
SiO_2@CDs@MIM	0.05–0.4	—	Deionized water	FRET	Human plasma	53
CuNCs	0.001724–0.02586	97	Distilled water	Complex formation	Human plasma samples	55
NPCDs	0.5–6.5	17.2	Distilled water	Static quenching and IFE	Human urine and serum samples	57
PCQDs	1–30 and 30–70	2.84	Ethanol	IFE	Human urine and serum samples	58
PEI-CDs	0.1–150	22.88	Deionized water	IFE	Human urine samples	59
UCNPs	0.0862–34.48 and 34.48–258.62	—	Deionized water	IFE	Human serum samples	64
CC/DTT-AuNCs	0.05–2	—	Water	PET	Human serum samples	65
Apt-UCNPs	0.5–55	0.3	DMSO	FRET	Human urine samples	144
N-CDs	0.1–1.5 and 4–110	18	Millipore water	IFE	Human blood serum	145
PEG-UCNPs	0–0.68967 and 17.24–172.42	—	Normal saline	FRET	Mice blood	146
CTC						
NEDA-CQDs	**0–90**	**2.7**	**Distilled water**	**Static quenching and IFE**	**Human serum and urine samples**	**Present Work**
CCNDs	0.1–15	—	Deionized water	Complex formation and AIE	A549 cell line, chicken, and feed samples	66
PEI-OVA-AuNCs	1–65	9.0	Water	IFE and AIQ	Tap and river water	67
TPE@CLMOF	0–160	63.2	Methanol, ethanol	Electron transfer and IFE	Honey samples	71
SiC@ZIF-8@MIP	0.194–34.93	—	Double distilled water	IFE and AIE	Milk and pig liver samples	74
$AgInS_2$ QDs	0.05–5.00	—	Ultrapure water	Electrostatic interactions and bandgap transitions	Milk, honey, and astragalus membranaceus samples	75
N, P-Ti_3C_2 QDs	2–22	3.79	Deionized water	Complex formation	Milk samples	76
N-CDs	0.0388–2.33	—	Ethanol	FRET	Actual water samples	77
N-CD	0.8–42	22.96	Ultrapure water	IFE	Pork samples	79
g-C_3N_4/MIP	0.04–2	—	Water	Charge transfer, static quenching, and electrostatic interaction	Milk sample	147
CuNC-Al^{3+}	0.1–3	—	Water	AIE	Environmental water and milk samples	148
Zn-BTEC MOF	0–8	—	Ultrapure water	AIE	Urine and fish samples	149
DECD	0.25–25	—	Deionized water	FRET and complex formation	Milk and eye ointment	150

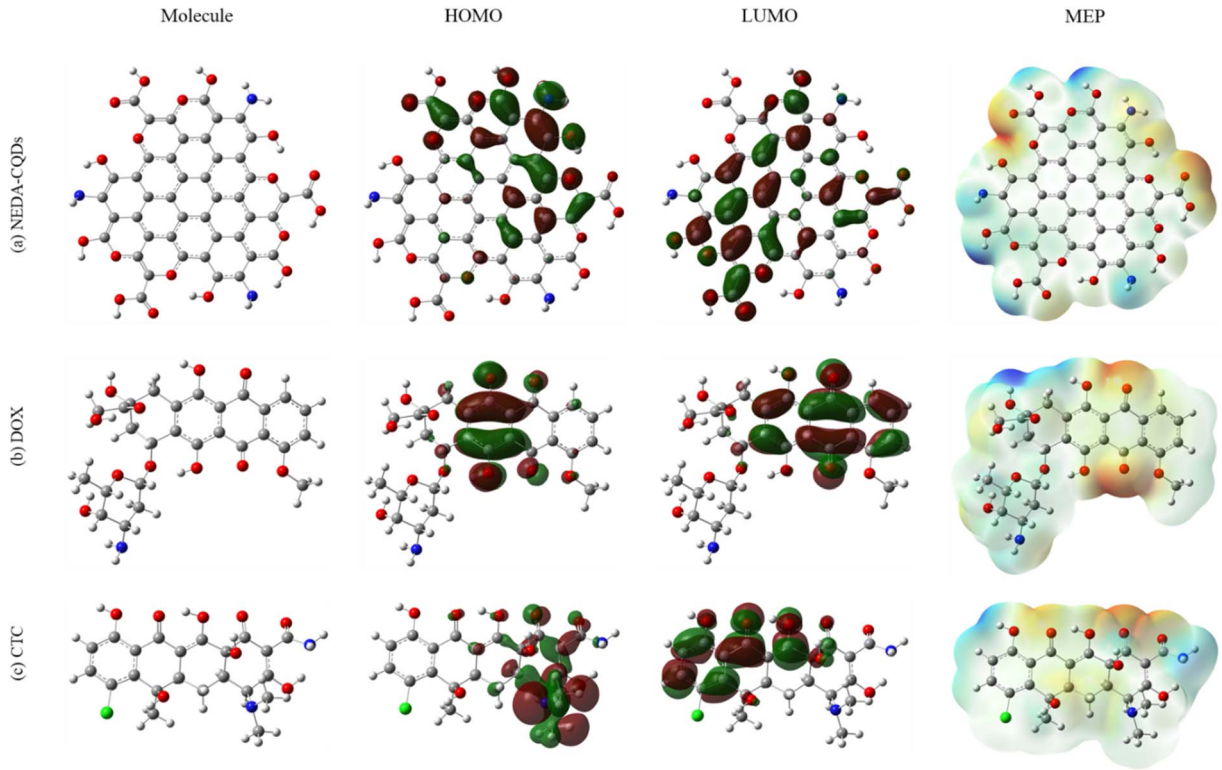

Fig. 7 The optimized geometry, spatial diagram of the HOMO, LUMO orbitals, and MEP analysis for (a) NEDA-CQDs nanosheet, (b) DOX, and (c) CTC drug molecules, respectively.

chemical composition and electronic behavior of the synthesized sensor.

This approach ensures that the calculated electronic properties, specifically the Molecular Electrostatic Potential (MEP) and the frontier molecular orbital distribution (HOMO and LUMO), accurately represent the chemically active and polar surface of the synthesized material, validating the relevance of the computed non-covalent interactions (NCI) with the drug molecules. The Density Functional Theory (DFT) calculations provide crucial insights into the electronic structure and binding mechanism between the NEDA-CQDs and the drug molecules DOX and CTC, which are relevant for understanding their potential as a drug sensor.

3.10.1. The structural and electronic characteristics of the NEDA-CQDs nanosheet, DOX, and CTC drug molecules. The optimized structure of the NEDA-CQDs nanosheet, as shown in Fig. 7(a), displayed a well-delocalized π-conjugated system presented by the polyaromatic core, which is essential for efficient electronic transfer with drug molecules. The plots for the HOMO and LUMO illustrate the electron distribution and potential sites for chemical reactions. According to the NEDA-CQDs, the HOMO density was largely localized over the aromatic carbon network, while the LUMO extended across the same surface, indicating that the entire carbon core is electronically active. The MEP map revealed the presence of electron-rich (red/negative) and electron-deficient (blue/

Table 3 The calculated value of the binding energy (E_{bind}), HOMO energy (E_{HOMO}), LUMO energy (E_{LUMO}), HOMO–LUMO energy gap (E_g), change in E_g (ΔE_g), Fermi level energy (E_F), change in E_F (ΔE_F), and dipole moment (D) of the NEDA-CQDs nanosheet before and after interaction with DOX and CTC drug molecules in vacuum, respectively

System	E_{bind} (eV)	E_{HOMO} (eV)	E_{LUMO} (eV)	E_g (eV)	ΔE_g (%)	E_F (eV)	ΔE_F (%)	D (debye)
Molecule								
DOX	—	−5.64	−2.16	3.49	—	−3.90	—	3.61
CTC	—	−5.73	−1.84	3.88	—	−3.79	—	4.05
NEDA-CQDs	—	−4.14	−2.38	1.76	0.00	−3.26	0.00	9.37
Complex								
DOX/NEDA-CQDs	−3.07	−4.11	−2.54	1.57	−10.55	−3.33	2.03	7.99
CTC/NEDA-CQDs	−3.08	−4.28	−2.60	1.68	−4.24	−3.44	5.39	4.17

positive) domains for nucleophilic and electrophilic attack. NEDA-CQDs show a mixture of negative potential near the oxygen and nitrogen-containing functional groups and some positive potential over the carbon structure. These sites act as the primary binding centers for the targeted drugs.

Additionally, the calculated total Mulliken charge of the sensor is 0.00e, and the dipole moment (D) is 9.37 debye. Different quantum chemical parameters, including HOMO energy (E_{HOMO}), LUMO energy (E_{LUMO}), the HOMO–LUMO energy gap (E_g), Fermi level energy (E_F), and D, were obtained and are summarized in Table 3. The computed E_g value is 1.76 eV (using eqn (2)), reflecting a relatively narrow band-gap suitable for electron transfer processes, which is consistent with the close energy levels in the density of states (DOS) spectra displayed in Fig. 9(a). Additionally, the Fermi level (E_F) was determined to be −3.26 eV based on eqn (4).

The optimized geometries of DOX and CTC drug molecules are presented in Fig. 7(b and c). The HOMO and LUMO are primarily localized on the polyaromatic rings (the chromophore), which is expected due to the π-system's role in electron delocalization. The presence of heteroatoms (O, N, Cl) also influences the distribution. According to the MEP map, both drugs display distinct negative regions around the oxygen atoms of the carbonyl and hydroxyl groups, which are potential sites for hydrogen bonding with the NEDA-CQD's surface groups.

Furthermore, both drug molecules exhibit a total Mulliken charge of 0.00e, confirming their charge neutrality. The E_g values of DOX and CTC, calculated using eqn (2), are 3.49 eV and 3.88 eV, respectively, which is further validated by their corresponding DOS spectra shown in Fig. S4(a and b) in the supplementary information section.

3.10.2. The optimized orientation for the binding of the DOX and CTC drug molecules over the NEDA-CQDs nanosheet. The optimized geometries of the drug–sensor complexes, as presented in Fig. 8(a and b), reveal that both DOX and CTC adopt a nearly parallel alignment with the NEDA-CQDs nanosheet during the binding. DOX occupies the central surface region of NEDA-CQDs, while CTC binds at the edges or near heteroatom sites. This parallel orientation maximizes surface contact and facilitates strong π–π interactions between the aromatic domains of the drugs and the conjugated sp^2-carbon network of the CQDs. In addition to π–π stacking, several hydrogen bonds are formed between the drug functional groups (such as OH, NH, C═O) and the oxygen- and nitrogen-containing surface groups of the nanosheet. The coexistence of aromatic stacking and hydrogen-bonding interactions creates a stable binding configuration, promotes efficient electronic coupling, and supports the observed charge-transfer–driven fluorescence quenching mechanism.

Upon complexation, the electronic distribution is significantly altered, particularly in the HOMO and LUMO of the drug complexes. In both complexes, the HOMO remains primarily localized on the NEDA-CQDs nanosheet, while the LUMO shifts significantly towards the drug molecules (DOX/CTC). This spatial separation of the frontier orbitals suggests an electron transfer from the NEDA-CQDs (acting as an electron donor) to the drug molecules (acting as an electron acceptor). This charge transfer is a critical driving force for the stable formation of the complexes and could influence the photophysical properties and stability. This orbital alignment supports an inner-filter effect (IFE)-assisted quenching mechanism.

MEP maps revealed highly intensified negative electrostatic potential around the carbonyl and hydroxyl groups of DOX and CTC, enabling strong hydrogen bonding and electrostatic interactions with the positively polarized N–H and C–H sites on the NEDA-CQDs surface. In both complexes, these polar interactions are complemented by π–π stacking, as the drugs adopt a nearly parallel orientation relative to the CQD nanosheet. This electrostatic stabilization, hydrogen bonding combined with aromatic π–π interactions, promotes efficient electronic coupling and facilitates intermolecular charge transfer, ultimately supporting the experimentally observed fluorescence quenching mechanism of the NEDA-CQDs sensor in the presence of DOX and CTC.

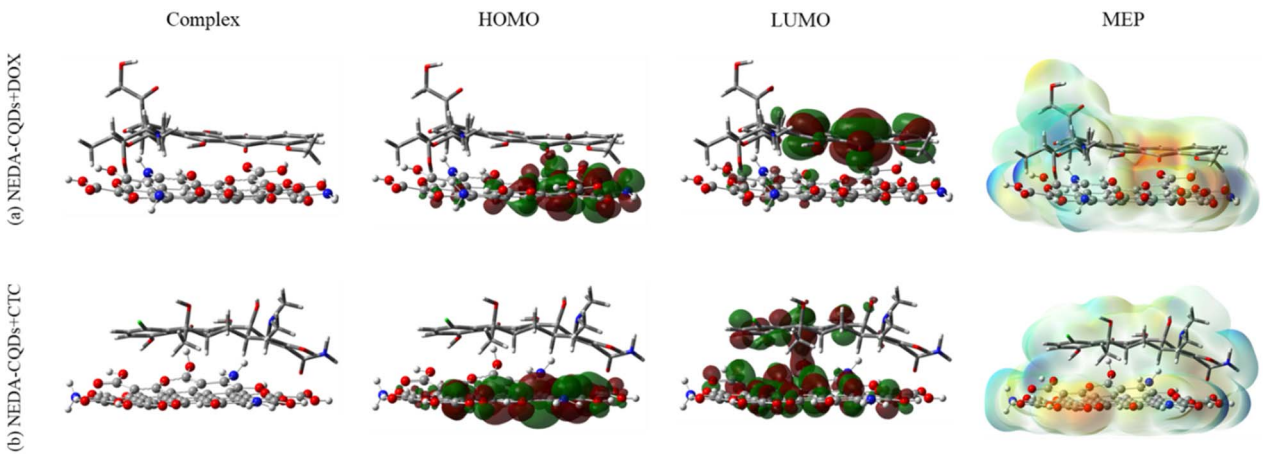

Fig. 8 The optimized structure, spatial diagram of the HOMO, LUMO orbitals, and MEP analysis for (a) DOX/NEDA-CQDs and (b) CTC/NEDA-CQDs drug complexes, respectively.

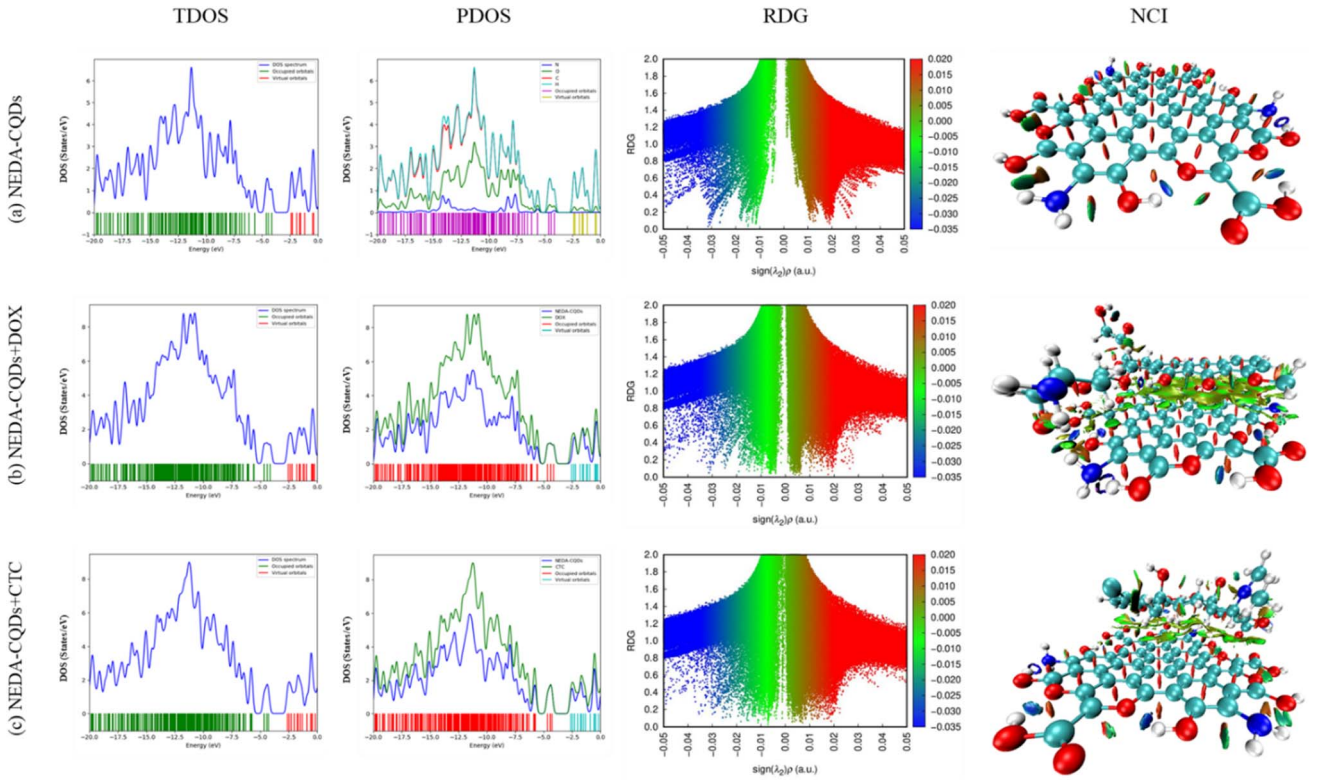

Fig. 9 The TDOS spectra, PDOS spectra, RDG plot, and NCI iso-surfaces diagrams for (a) NEDA-CQDs nanosheet, (b) DOX/NEDA-CQDs, and (c) CTC/NEDA-CQDs drug complexes, respectively.

Additionally, the binding energies (E_{bind}) of the two drug molecules on the NEDA-CQDs nanosheet were calculated to assess the strength and stability of the interactions. Using eqn (1), the E_{bind} values for the DOX/NEDA-CQDs and CTC/NEDA-CQDs complexes were determined to be −3.07 and −3.08 eV, respectively. These strong negative binding energies confirm that both drugs form favorable and stable complexes with the sensor surface.

The density of states (DOS) spectra, together with the electronic parameters E_{HOMO}, E_{LUMO}, energy gap (E_g), its variation (ΔE_g), Fermi level energy (E_F), its shift (ΔE_F), and the dipole moment (D), were examined after binding of the drug molecules onto the NEDA-CQDs surface, as presented in Table 3. The DOS spectra of the nanosheet in the presence of DOX and CTC are shown in Fig. 9(b and c). The observed alterations in the orbital distributions following drug binding provide further evidence of strong electronic interactions between the drug molecules and the NEDA-CQDs sensor.

The pristine NEDA-CQDs nanosheet displays an energy gap (E_g) of 1.76 eV, as determined from eqn (2), with corresponding E_{HOMO} and E_{LUMO} values of −4.14 and −2.38 eV, respectively. After binding of DOX and CTC onto the sensor surface, these orbital energies shift to −4.11 and −4.28 eV for E_{HOMO} and −2.54 and −2.60 eV for E_{LUMO}, leading to reduced energy gaps of 1.57 and 1.68 eV, respectively. The Fermi energy (E_F), calculated using eqn (4), also shifts to −3.33 eV for the DOX/NEDA-CQDs complex and −3.44 eV for the CTC/NEDA-CQDs complex. These modifications in E_{HOMO}, E_{LUMO}, E_g, and E_F closely align with the changes observed in the DOS spectra, confirming notable alterations in the electronic structure of the nanosheet induced by drug binding. Such shifts further indicate strong interaction and efficient electronic coupling between the drugs and the NEDA-CQDs surface.

3.10.3. Reduced density gradient (RDG) plots and non-covalent interaction (NCI) analysis. The NCI/RDG analysis is the most informative for visualizing and characterizing the non-covalent forces. The NCI plots use color-coded iso-surfaces to map different interaction strengths between the CQD and the drug.

RDG scatter plots further support the results by displaying distinct regions corresponding to weak non-covalent interactions upon drug binding. In both DOX- and CTC-bound structures, as displayed in Fig. 9(a–c), the appearance of spikes in the low-density, low-gradient region indicates stabilizing interactions such as hydrogen bonding and van der Waals forces. The presence of additional colored regions compared to the pristine CQDs confirms that drug binding introduces new non-covalent contact zones that enhance complex stability.

The NCI *iso*-surfaces provide direct visualization of these interactions, showing extended green regions between the aromatic rings of the drugs and the conjugated domains of the CQDs, which correspond to π–π stacking interactions. Blue-green patches localized around the drug functional groups (C═O, OH, COOH) and the NEDA-CQDs surface functional groups (N–H, C–H, C–O) confirm the formation of multiple hydrogen bonds. The combination of π–π stacking and

Table 4 The calculated values of the work function (φ), ionization potential (I), electron affinity (A), electronegativity (χ), chemical potential (μ), hardness (η), softness (S), and electrophilicity index (ω) of the NEDA-CQDs nanosheet, DOX/NEDA-CQDs, and CTC/NEDA-CQDs drug complexes in vacuum, respectively

System	φ (eV)	I (eV)	A (eV)	χ (eV)	μ (eV)	η (eV)	S $(eV)^{-1}$	ω (eV)
Molecule								
DOX	3.90	5.64	2.16	3.90	−3.90	1.74	1.15	4.36
CTC	3.79	5.73	1.84	3.79	−3.79	1.94	1.03	3.69
NEDA-CQDs	3.26	4.14	2.38	3.26	−3.26	0.88	2.27	6.05
Complex								
DOX/NEDA-CQDs	3.33	4.11	2.54	3.33	−3.33	0.79	2.54	7.04
CTC/NEDA-CQDs	3.44	4.28	2.60	3.44	−3.44	0.84	2.37	7.02

hydrogen bonding leads to stable binding geometries in which both drugs lie nearly parallel to the nanosheet surface, maximizing contact and facilitating effective charge transfer.

Overall, the DFT results collectively demonstrate that NEDA-CQDs are capable of forming stable complexes with both DOX and CTC. The binding is governed by a cooperative effect of strong π–π stacking and hydrogen bonding, confirmed by the RDG and NCI analysis. The findings support the potential application of NEDA-CQDs as an effective sensor for these chemotherapeutic and antibiotic agents.

3.10.4. Chemical reactivity descriptors. The quantum chemical descriptors listed in Table 4 provide valuable insight into the electronic properties and reactivity of the pristine NEDA-CQDs nanosheet and its complexes with DOX and CTC. Several reactivity descriptors were calculated using the standard conceptual DFT equations, including work function (φ), ionization potential (I), electron affinity (A), electronegativity (χ), chemical potential (μ), chemical hardness (η), softness (S), and electrophilicity index (ω). Their respective expressions are given by:

$$\varphi = V_{el(+\alpha)} - E_F \quad (9)$$

$$\mu = -\chi = -\frac{(I + A)}{2} \quad (10)$$

$$\eta = \frac{(I - A)}{2} \quad (11)$$

$$S = \frac{1}{2\eta} \quad (12)$$

$$\omega = \frac{\mu^2}{2\eta} \quad (13)$$

In this context, the ionization energy (I) is defined as $-E_{HOMO}$, and the electron affinity (A) is defined as $-E_{LUMO}$, meaning that $I \approx -E_{HOMO}$ and $A \approx -E_{LUMO}$. These quantities were calculated directly from the HOMO and LUMO energy levels of the NEDA-CQDs nanosheet and its complexes with the DOX and CTC drug molecules. Using these relationships, the pristine NEDA-CQDs exhibit moderate electronegativity ($\chi = 3.26$ eV), relatively low ionization potential ($I = 4.14$ eV), and high softness ($S = 2.27$ eV^{-1}), indicating that the nanosheet is chemically reactive and capable of efficient electron exchange. The work function ($\varphi = 3.26$ eV) further confirms its ability to donate electrons easily.

Upon binding of DOX and CTC drugs, noticeable electronic changes occur in these descriptors, indicating strong electronic interactions between the NEDA-CQDs surface and the drug molecules. Both complexes show a slight increase in work function (3.33 eV for DOX/NEDA-CQDs and 3.44 eV for CTC/NEDA-CQDs), implying a shift in the surface Fermi level due to charge redistribution. This enhancement in φ indicates that electron removal becomes slightly more energy-demanding, consistent with the formation of a more electronically stabilized interface.

The ionization potential (I) and electron affinity (A) also increase for both complexes compared to the pristine NEDA-CQDs nanosheet, indicating enhanced charge-accepting and charge-donating capabilities after drug binding. As a result, the chemical hardness (η) decreases from 0.88 eV for NEDA-CQDs to 0.79 and 0.84 eV for DOX/NEDA-CQDs and CTC/NEDA-CQDs complexes, while softness (S) increases. These changes indicate that the nanosheet becomes more chemically responsive upon drug binding, facilitating electron transfer interactions between the drug molecules and the nanosheet, an essential feature for sensing performance.

Electronegativity (χ) and chemical potential (μ) also show a slight increase in their values, demonstrating that the complexes possess a greater tendency to attract electrons and enhancing the interaction strength between the drugs and NEDA-CQDs. Most notably, the electrophilicity index (ω) increases significantly upon complexation from 6.05 eV for pristine NEDA-CQDs to 7.04 eV (DOX/NEDA-CQDs) and 7.02 eV (CTC/NEDA-CQDs). The higher ω values indicate that both complexes exhibit enhanced stabilization energy upon electron acceptance, confirming a strong electrophilic character. This enhancement is directly associated with improved sensing capability, as higher electrophilicity facilitates more efficient electron exchange between the drug molecules and the nanosheet surface.

Overall, these changes in the global reactivity descriptors confirm that DOX and CTC binding onto NEDA-CQDs induce substantial electronic modulation of the nanosheet. The increased softness, electrophilicity, and work function of the complexes confirm enhanced charge-transfer interactions,

supporting the excellent performance of the NEDA-CQDs as a fluorescence-based sensor for DOX and CTC detection.

4. Conclusion

In this work, nitrogen-rich NEDA-CQDs were successfully synthesized *via* a simple one-step hydrothermal strategy and employed as a dual-function fluorescent sensor for the detection of DOX and CTC. The obtained carbon quantum dots exhibited uniform nanoscale dimensions, good aqueous stability, and excitation-independent fluorescence behavior suitable for sensing applications. The developed platform enabled concentration-dependent fluorescence quenching over a wide linear range (0–90 μM) for both analytes, with satisfactory sensitivity, selectivity, stability, and reproducibility. Importantly, the sensor demonstrated reliable performance in spiked human serum and urine samples, confirming its practical applicability in biological matrices without complicated sample pretreatment.

Mechanistic investigations revealed that the sensing process is governed by static quenching accompanied by the IFE. DFT calculations provided theoretical validation of the experimental findings, demonstrating strong binding interactions, charge redistribution, reduced HOMO–LUMO energy gaps, and favorable non-covalent interactions, particularly π–π stacking and hydrogen bonding, between the drug molecules and the NEDA-CQDs surface.

Compared with previously reported fluorescent probes, the present system offers several advantages, including dual-analyte detection using a single sensing platform, simple and cost-effective synthesis, mechanistic insight supported by theoretical calculations, and successful validation in real biofluids. These combined features highlight the potential of NEDA-CQDs as a practical and versatile fluorescent platform for pharmaceutical monitoring and bioanalytical applications.

Ethics statement

All experiments were performed in compliance with relevant laws and institutional guidelines. The experimental protocol was approved by the Ethics Committee of Damietta university. Informed consent was obtained from all human subjects participating in this study.

Author contributions

Sondos Lotfy: computational analysis, investigation, data curation, visualization, formal analysis, methodology, writing – original draft. Mohamed M. Aboelnga: supervision, validation, conceptualization, project administration, computational analysis, investigation, visualization, data analysis, software, resources, writing – review & editing. Elhossein A. Moawed: supervision, validation, conceptualization, project administration, writing – review & editing. Elsayed Elbayoumy: supervision, validation, conceptualization, project administration, writing – review & editing, resources, investigation, formal analysis, data curation.

Conflicts of interest

The authors declare that they have no known competing financial interests or personal relationships that could have appeared to influence the work reported in this paper.

Data availability

The data that support the findings of this study are available from the corresponding author upon reasonable request.

Supplementary information (SI) is available. See DOI: https://doi.org/10.1039/d6na00019c.

Acknowledgements

We thank the central laboratory at the Faculty of Science, Damietta University, for providing the facilities to conduct UV-vis and fluorescence spectroscopy analysis.

References

1 F. L. Short, V. Lee, R. Mamun, R. Malmberg, L. Li, M. I. Espinosa, K.-I. Abbu, J. Algie, A. Callaghan, P. Cenderawasih-Nere, V. Cullen, M. Gooden, M. Kanoun, A. Lawrie, J. Maher, V. Malek, Z. Safdari, B. Shehadie, S.-Y. Shifa, I. Simpson, M. Towns, S. Valter, K. Venkatesan and I. T. Paulsen, Benzalkonium chloride antagonises aminoglycoside antibiotics and promotes evolution of resistance, *EBioMedicine*, 2021, **73**, 103653.

2 O. I. Guliy, B. D. Zaitsev, A. V. Smirnov, O. A. Karavaeva and I. A. Borodina, Prospects of acoustic sensor systems for antibiotic detection, *Biosens. Bioelectron.:X*, 2022, **12**, 100274.

3 J. Hou, X. Long, X. Wang, L. Li, D. Mao, Y. Luo and H. Ren, Global trend of antimicrobial resistance in common bacterial pathogens in response to antibiotic consumption, *J. Hazard. Mater.*, 2023, **442**, 130042.

4 D. S. Gupta and M. S. Kumar, The implications of quorum sensing inhibition in bacterial antibiotic resistance- with a special focus on aquaculture, *J. Microbiol. Methods*, 2022, **203**, 106602.

5 W. Qiu, B. Chen, L. Tang, C. Zheng, B. Xu, Z. Liu, J. T. Magnuson, S. Zhang, D. Schlenk, E. G. Xu and B. Xing, Antibiotic Chlortetracycline Causes Transgenerational Immunosuppression via NF-κB, *Environ. Sci. Technol.*, 2022, **56**, 4251–4261.

6 S. Hong, T. J. Moritz, C. M. Rath, P. Tamrakar, P. Lee, T. Krucker and L. P. Lee, Assessing Antibiotic Permeability of Gram-Negative Bacteria *via* Nanofluidics, *ACS Nano*, 2017, **11**, 6959–6967.

7 S. A. Kelly, J. Nzakizwanayo, A. M. Rodgers, L. Zhao, R. Weiser, I. A. Tekko, H. O. McCarthy, R. J. Ingram, B. V. Jones, R. F. Donnelly and B. F. Gilmore, Antibiotic Therapy and the Gut Microbiome: Investigating the Effect of Delivery Route on Gut Pathogens, *ACS Infect. Dis.*, 2021, **7**, 1283–1296.

8 S. A. R. Alavi-Tabari, M. A. Khalilzadeh and H. Karimi-Maleh, Simultaneous determination of doxorubicin and dasatinib as two breast anticancer drugs uses an amplified sensor with ionic liquid and ZnO nanoparticle, *J. Electroanal. Chem.*, 2018, **811**, 84–88.

9 R. Venkatesan, A. Pichaimani, K. Hari, P. K. Balasubramanian, J. Kulandaivel and K. Premkumar, Doxorubicin conjugated gold nanorods: a sustained drug delivery carrier for improved anticancer therapy, *J. Mater. Chem. B*, 2013, **1**, 1010–1018.

10 G. R. Chamberlain, D. V. Tulumello and S. O. Kelley, Targeted Delivery of Doxorubicin to Mitochondria, *ACS Chem. Biol.*, 2013, **8**, 1389–1395.

11 B. Cerroni, E. Chiessi, S. Margheritelli, L. Oddo and G. Paradossi, Polymer Shelled Microparticles for a Targeted Doxorubicin Delivery in Cancer Therapy, *Biomacromolecules*, 2011, **12**, 593–601.

12 F. Chekin, V. Myshin, R. Ye, S. Melinte, S. K. Singh, S. Kurungot, R. Boukherroub and S. Szunerits, Graphene-modified electrodes for sensing doxorubicin hydrochloride in human plasma, *Anal. Bioanal. Chem.*, 2019, **411**, 1509–1516.

13 R. Sultana, F. Di Domenico, M. Tseng, J. Cai, T. Noel, R. L. Chelvarajan, W. D. Pierce, C. Cini, S. Bondada, D. K. St. Clair and D. A. Butterfield, Doxorubicin-Induced Thymus Senescence, *J. Proteome Res.*, 2010, **9**, 6232–6241.

14 C. Carvalho, R. Santos, S. Cardoso, S. Correia, P. Oliveira, M. Santos and P. Moreira, Doxorubicin: The Good, the Bad and the Ugly Effect, *Curr. Med. Chem.*, 2009, **16**, 3267–3285.

15 R. Pulicharla, S. K. Brar, T. Rouissi, S. Auger, P. Drogui, M. Verma and R. Y. Surampalli, Degradation of chlortetracycline in wastewater sludge by ultrasonication, Fenton oxidation, and ferro-sonication, *Ultrason. Sonochem.*, 2017, **34**, 332–342.

16 Y. Zhou, L. Niu, S. Zhu, H. Lu and W. Liu, Occurrence, abundance, and distribution of sulfonamide and tetracycline resistance genes in agricultural soils across China, *Sci. Total Environ.*, 2017, **599–600**, 1977–1983.

17 S. Croubels, C. Van Peteghem and W. Baeyens, Sensitive spectrofluorimetric determination of tetracycline residues in bovine milk, *Analyst*, 1994, **119**, 2713.

18 K. De Wasch, L. Okerman, H. De Brabander, J. Van Hoof, S. Croubels and P. De Backer, Detection of residues of tetracycline antibiotics in pork and chicken meat: correlation between results of screening and confirmatory tests†, *Analyst*, 1998, **123**, 2737–2741.

19 M. Jeon and I. Rhee Paeng, Quantitative detection of tetracycline residues in honey by a simple sensitive immunoassay, *Anal. Chim. Acta*, 2008, **626**, 180–185.

20 J. A. Rodriguez, J. Espinosa, K. Aguilar-Arteaga, I. S. Ibarra and J. M. Miranda, Determination of tetracyclines in milk samples by magnetic solid phase extraction flow injection analysis, *Microchim. Acta*, 2010, **171**, 407–413.

21 F. Yuan, H. Zhao, Z. Zhang, L. Gao, J. Xu and X. Quan, Fluorescent biosensor for sensitive analysis of oxytetracycline based on an indirectly labelled long-chain aptamer, *RSC Adv.*, 2015, **5**, 58895–58901.

22 R. Pulicharla, R. K. Das, S. K. Brar, P. Drogui, S. J. Sarma, M. Verma, R. Y. Surampalli and J. R. Valero, Toxicity of chlortetracycline and its metal complexes to model microorganisms in wastewater sludge, *Sci. Total Environ.*, 2015, **532**, 669–675.

23 M. H. Khan and J.-Y. Jung, Ozonation of chlortetracycline in the aqueous phase: Degradation intermediates and pathway confirmed by NMR, *Chemosphere*, 2016, **152**, 31–38.

24 J. Han, J. Zhang, H. Zhao, Y. Li and Z. Chen, Simultaneous determination of doxorubicin and its dipeptide prodrug in mice plasma by HPLC with fluorescence detection, *J. Pharm. Anal.*, 2016, **6**, 199–202.

25 M. Gros, S. Rodríguez-Mozaz and D. Barceló, Rapid analysis of multiclass antibiotic residues and some of their metabolites in hospital, urban wastewater and river water by ultra-high-performance liquid chromatography coupled to quadrupole-linear ion trap tandem mass spectrometry, *J. Chromatogr. A*, 2013, **1292**, 173–188.

26 P. Moudgil, J. S. Bedi, R. S. Aulakh, J. P. S. Gill and A. Kumar, Validation of HPLC Multi-residue Method for Determination of Fluoroquinolones, Tetracycline, Sulphonamides and Chloramphenicol Residues in Bovine Milk, *Food Anal. Methods*, 2019, **12**, 338–346.

27 M. Shah, L. Bourner, S. Ali, S. Al-Enazy, M. Youssef, M. Fisler and E. Rytting, HPLC Method Development for Quantification of Doxorubicin in Cell Culture and Placental Perfusion Media, *Separations*, 2018, **5**, 9.

28 J. K. Lukowski and A. B. Hummon, Quantitative evaluation of liposomal doxorubicin and its metabolites in spheroids, *Anal. Bioanal. Chem.*, 2019, **411**, 7087–7094.

29 A. Pollap and J. Kochana, Electrochemical Immunosensors for Antibiotic Detection, *Biosensors*, 2019, **9**, 61.

30 P. M. Alizadeh, M. Hasanzadeh, J. Soleymani, J. V. Gharamaleki and A. Jouyban, Application of bioactive cyclic oligosaccharide on the detection of doxorubicin hydrochloride in unprocessed human plasma sample: A new platform towards efficient chemotherapy, *Microchem. J.*, 2019, **145**, 450–455.

31 X. Yang, H. Gao, F. Qian, C. Zhao and X. Liao, Internal standard method for the measurement of doxorubicin and daunorubicin by capillary electrophoresis with in-column double optical-fiber LED-induced fluorescence detection, *J. Pharm. Biomed. Anal.*, 2016, **117**, 118–124.

32 Y. Tang, H. Huang, W. Xue, Y. Chang, Y. Li, X. Guo and C. Zhong, Rigidifying induced fluorescence enhancement in 2D porous covalent triazine framework nanosheets for the simultaneously luminous detection and adsorption removal of antibiotics, *Chem. Eng. J.*, 2020, **384**, 123382.

33 M. Yang, Y. Yan, H. Shi, C. Wang, E. Liu, X. Hu and J. Fan, Efficient inner filter effect sensors based on CdTeS quantum dots and Ag nanoparticles for sensitive detection of l-cysteine, *J. Alloys Compd.*, 2019, **781**, 1021–1027.

34 H.-H. Chung, J.-B. Lee, Y.-H. Chung and K.-G. Lee, Analysis of sulfonamide and quinolone antibiotic residues in Korean milk using microbial assays and high performance liquid chromatography, *Food Chem.*, 2009, **113**, 297–301.
35 M. Han, L. Gong, J. Wang, X. Zhang, Y. Jin, R. Zhao, C. Yang, L. He, X. Feng and Y. Chen, An octuplex lateral flow immunoassay for rapid detection of antibiotic residues, aflatoxin M1 and melamine in milk, *Sens. Actuators, B*, 2019, **292**, 94–104.
36 E. Song, M. Yu, Y. Wang, W. Hu, D. Cheng, M. T. Swihart and Y. Song, Multi-color quantum dot-based fluorescence immunoassay array for simultaneous visual detection of multiple antibiotic residues in milk, *Biosens. Bioelectron.*, 2015, **72**, 320–325.
37 Q. Hu, L. Gao, S. Rao, Z. Yang, T. Li and X. Gong, Nitrogen and chlorine dual-doped carbon nanodots for determination of curcumin in food matrix via inner filter effect, *Food Chem.*, 2019, **280**, 195–202.
38 Y. Qu, G. Ren, L. Yu, B. Zhu, F. Chai and L. Chen, The carbon dots as colorimetric and fluorescent dual-readout probe for 2-nitrophenol and 4-nitrophenol detection, *J. Lumin.*, 2019, **207**, 589–596.
39 A. Concellón, J. Castro-Esteban and T. M. Swager, Ultratrace PFAS Detection Using Amplifying Fluorescent Polymers, *J. Am. Chem. Soc.*, 2023, **145**, 11420–11430.
40 A. Zhu, Q. Qu, X. Shao, B. Kong and Y. Tian, Carbon-Dot-Based Dual-Emission Nanohybrid Produces a Ratiometric Fluorescent Sensor for In Vivo Imaging of Cellular Copper Ions, *Angew. Chem., Int. Ed.*, 2012, **51**, 7185–7189.
41 A. Zhu, Z. Luo, C. Ding, B. Li, S. Zhou, R. Wang and Y. Tian, A two-photon "turn-on" fluorescent probe based on carbon nanodots for imaging and selective biosensing of hydrogen sulfide in live cells and tissues, *Analyst*, 2014, **139**, 1945–1952.
42 P. Wang, T.-H. Wu and Y. Zhang, Novel silver nanoparticle-enhanced fluorometric determination of trace tetracyclines in aqueous solutions, *Talanta*, 2016, **146**, 175–180.
43 Y. Wang, P. Ni, S. Jiang, W. Lu, Z. Li, H. Liu, J. Lin, Y. Sun and Z. Li, Highly sensitive fluorometric determination of oxytetracycline based on carbon dots and Fe3O4 MNPs, *Sens. Actuators, B*, 2018, **254**, 1118–1124.
44 Y. Zhou, Q. Yang, D. Zhang, N. Gan, Q. Li and J. Cuan, Detection and removal of antibiotic tetracycline in water with a highly stable luminescent MOF, *Sens. Actuators, B*, 2018, **262**, 137–143.
45 Z. Zhou, K. Lu, X. Wei, T. Hao, Y. Xu, X. Lv and Y. Zhang, A mesoporous fluorescent sensor based on ZnO nanorods for the fluorescent detection and selective recognition of tetracycline, *RSC Adv.*, 2016, **6**, 71061–71069.
46 Z. Xu, X. Yi, Q. Wu, Y. Zhu, M. Ou and X. Xu, First report on a BODIPY-based fluorescent probe for sensitive detection of oxytetracycline: application for the rapid determination of oxytetracycline in milk, honey and pork, *RSC Adv.*, 2016, **6**, 89288–89297.
47 F. Martínez Ferreras, O. S. Wolfbeis and H. H. Gorris, Dual lifetime referenced fluorometry for the determination of doxorubicin in urine, *Anal. Chim. Acta*, 2012, **729**, 62–66.
48 J. Dong, K. Wang, L. Sun, B. Sun, M. Yang, H. Chen, Y. Wang, J. Sun and L. Dong, Application of graphene quantum dots for simultaneous fluorescence imaging and tumor-targeted drug delivery, *Sens. Actuators, B*, 2018, **256**, 616–623.
49 H. Liu, J. Qiu, R. Zhang, J. Li, Y. Sang, W. Tang and P. Rivera Gil, Fluorescent graphene quantum dots as traceable, pH-sensitive drug delivery systems, *Int. J. Nanomed.*, 2015, 6709.
50 G. Mi, H. Shi, M. Yang, C. Wang, H. Hao and J. Fan, Efficient detection doxorubicin hydrochloride using CuInSe2@ZnS quantum dots and Ag nanoparticles, *Spectrochim. Acta, Part A*, 2020, **241**, 118673.
51 S. A. Mescheryakova, I. S. Matlakhov, P. D. Strokin, D. D. Drozd, I. Yu. Goryacheva and O. A. Goryacheva, Fluorescent Alloyed CdZnSeS/ZnS Nanosensor for Doxorubicin Detection, *Biosensors*, 2023, **13**, 596.
52 H. Zhang, F. Fang, J. Yi, Y. Sun and X. Wang, Molecularly imprinted polymer coupled with zinc-doped carbon quantum dots as a fluorescent probe for the determination of doxorubicin hydrochloride, *New J. Chem.*, 2025, **49**, 3200–3206.
53 Z. Xu, P. Deng, J. Li, L. Xu and S. Tang, Molecularly imprinted fluorescent probe based on FRET for selective and sensitive detection of doxorubicin, *Mater. Sci. Eng., B*, 2017, **218**, 31–39.
54 C. Chen, H.-D. Zhang, Y. Tao, L.-J. Liang, C. He, B.-C. Su, H.-Y. Li and F.-P. Huang, Tracking the Stepwise Formation of a Water-Soluble Fluorescent Tb_{12} Cluster for Efficient Doxorubicin Detection, *Inorg. Chem.*, 2022, **61**, 9385–9391.
55 M. S. Polat and H. Nadaroglu, Utilizing Copper Nanoclusters as a Fluorescent Probe for Quantitative Monitoring of Doxorubicin Anticancer Drug, *J. Fluoresc.*, 2024, **35**, 3507–3518.
56 F. Li, P. Fan, X. Chen, X. Lin, C. Liu, C. Hu, S. Yang and F. Xiao, A ratiometric fluorescence strategy based on copper nanoclusters/carbon dots for sensitive detection of doxorubicin, *Luminescence*, 2022, **37**, 868–875.
57 W. Zhang, R. Ma, S. Gu, L. Zhang, N. Li and J. Qiao, Nitrogen and phosphorus co-doped carbon dots as an effective fluorescence probe for the detection of doxorubicin and cell imaging, *Opt. Mater.*, 2022, **128**, 112323.
58 J. Zhu, H. Chu, J. Shen, C. Wang and Y. Wei, Green preparation of carbon dots from plum as a ratiometric fluorescent probe for detection of doxorubicin, *Opt. Mater.*, 2021, **114**, 110941.
59 M. Yang, Y. Yan, E. Liu, X. Hu, H. Hao and J. Fan, Polyethyleneimine-functionalized carbon dots as a fluorescent probe for doxorubicin hydrochloride by an inner filter effect, *Opt. Mater.*, 2021, **112**, 110743.
60 S. Swain, A. K. Jena and T. Mohanta, Ratiometric Fluorescence/Colorimetry/Smartphone Triple-Mode Real-

Time Detection of Doxorubicin by Nitrogen-Doped Carbon Dots, *ACS Appl. Opt. Mater.*, 2023, **1**, 1236–1244.

61 N. Gao, W. Yang, H. Nie, Y. Gong, J. Jing, L. Gao and X. Zhang, Turn-on theranostic fluorescent nanoprobe by electrostatic self-assembly of carbon dots with doxorubicin for targeted cancer cell imaging, in vivo hyaluronidase analysis, and targeted drug delivery, *Biosens. Bioelectron.*, 2017, **96**, 300–307.

62 J. Hu, R. Wang, R. Fan, Z. Huang, Y. Liu, G. Guo and H. Fu, Enhanced luminescence in Yb3+ doped core-shell upconversion nanoparticles for sensitive doxorubicin detection, *J. Lumin.*, 2020, **217**, 116812.

63 J. Mo, S. Wang, J. Zeng and X. Ding, Aptamer-based Upconversion Fluorescence Sensor for Doxorubicin Detection, *J. Fluoresc.*, 2023, **33**, 1897–1905.

64 Y. Chen, X. She, Z. Yang, C. Lu, W. Zhang, D. Feng, W. Wu and X. Wang, Preparation of upconversion NaYF4:Yb/Tm@NaYF4:Yb-Cit-CD for doxorubicin detection, *Opt. Mater.*, 2023, **135**, 113243.

65 K.-Y. Huang, H.-X. He, S.-B. He, X.-P. Zhang, H.-P. Peng, Z. Lin, H.-H. Deng, X.-H. Xia and W. Chen, Gold nanocluster-based fluorescence turn-off probe for sensing of doxorubicin by photoinduced electron transfer, *Sens. Actuators, B*, 2019, **296**, 126656.

66 Y.-X. Wu, H.-X. Huang, M.-A. Yang, Y. Sun, J. Xu, X. Ling, J.-P. Lai and H. Sun, A turn-on fluorescence sensor for highly selective detection of chlortetracycline based on AIE effect enhanced by citrate modified graphitic carbon nitride nanodots, *Microchem. J.*, 2024, **199**, 110180.

67 M. Li, N. Zhu, W. Zhu, S. Zhang, F. Li, P. Wu and X. Li, Enhanced emission and higher stability ovalbumin-stabilized gold nanoclusters (OVA-AuNCs) modified by polyethyleneimine for the fluorescence detection of tetracyclines, *Microchem. J.*, 2021, **169**, 106560.

68 L. Meng, C. Lan, Z. Liu, N. Xu and Y. Wu, A novel ratiometric fluorescence probe for highly sensitive and specific detection of chlorotetracycline among tetracycline antibiotics, *Anal. Chim. Acta*, 2019, **1089**, 144–151.

69 N. Bi, Y.-H. Xi, M.-H. Hu, J. Xu, J. Gou, Y.-X. Li, L.-N. Zhang and L. Jia, A sensitive multicolor fluorescence sensing strategy for chlorotetracycline based on bovine serum albumin-stabilized copper nanocluster, *Colloids Surf., B*, 2023, **228**, 113404.

70 X. Wang and S. Zhang, A highly selective fluorescent sensor for chlortetracycline based on histidine-templated copper nanoclusters, *Spectrochim. Acta, Part A*, 2022, **281**, 121588.

71 X. Sun, Y. Qiao, M. Zhang, Y. Cheng, F. Ning, H. Zhang and P. Hu, AIE-based cyclodextrin metal–organic frame material for fluorescence detection of nitrofuran and tetracycline antibiotics in aqueous solution, *Microchem. J.*, 2023, **190**, 108687.

72 Y. Ma, S. Wang, J. Guo, Z. Wang, H. Tang and K. Wang, Sensitive fluorescent detection of phosmet and chlortetracycline in animal-derived food samples based on a water-stable Cd(II) chain-based zwitterionic metal-organic framework, *Anal. Chim. Acta*, 2023, **1280**, 341850.

73 L. Yu, H. Chen, J. Yue, X. Chen, M. Sun, H. Tan, A. M. Asiri, K. A. Alamry, X. Wang and S. Wang, Metal–Organic Framework Enhances Aggregation-Induced Fluorescence of Chlortetracycline and the Application for Detection, *Anal. Chem.*, 2019, **91**, 5913–5921.

74 Y. Liu, Q. Chen, S. Li, Y. Cao, B. Zhang, G. Fang and S. Wang, Smartphone-assisted ratiometric fluorescent sensor for visual detection of chlortetracycline, *Food Chem.*, 2024, **460**, 140774.

75 W. Long, H. Lu, Y. Han, H. Chen, W. Lan, Y. She and H. Fu, Machine learning-assisted smartphone-based fluorescence visual sensing platform for ultrasensitive detection of chlortetracycline, *Sens. Actuators, B*, 2025, **428**, 137241.

76 R. Deng, Z. Wang, J. Chen, L. Zhu, Y. Shi and W. Xue, Rapid detection and differentiation of chlortetracycline and tetracycline by N,P-Ti3C2 QDs, *Microchem. J.*, 2024, **203**, 110854.

77 Z. Li, S. Li, L. Jiang, J. Xiao, J. Niu, Y. Zhang, C. Chen and Q. Zhou, Construction of nitrogen-doped carbon dots-based fluorescence probe for rapid, efficient and sensitive detection of chlortetracycline, *Chemosphere*, 2024, **361**, 142535.

78 Y.-S. Lee, C.-C. Hu and T.-C. Chiu, Electrochemical synthesis of fluorescent carbon dots for the selective detection of chlortetracycline, *J. Environ. Chem. Eng.*, 2022, **10**, 107413.

79 H. Zhang, Q. Zhou, X. Han, M. Li, J. Yuan, R. Wei, X. Zhang, M. Wu and W. Zhao, Nitrogen-doped carbon dots derived from hawthorn for the rapid determination of chlortetracycline in pork samples, *Spectrochim. Acta, Part A*, 2021, **255**, 119736.

80 X. Chen, J. Lin, Y. Zhuang, S. Huang, J. Chen and Z. Han, Dual-mode turn-on ratiometric fluorescence sensor based on carbon dots and CuInS2/ZnS quantum dots for detection of chlorotetracycline, *Spectrochim. Acta, Part A*, 2022, **270**, 120851.

81 C. Liu and G.-H. Cui, A stable luminescent Cd(II) coordination polymer for selective detection of chlortetracycline in aqueous medium, *Inorg. Chem. Commun.*, 2023, **150**, 110454.

82 L. Gao and J. Wang, A carbon quantum dot@mesoporous silicon composite-based fluorescent probe for chlortetracycline hydrochloride and gentamicin, *New J. Chem.*, 2025, **49**, 246–256.

83 Z. M. S. H. Khan, R. S. Rahman, Shumaila, S. Islam and M. Zulfequar, Hydrothermal treatment of red lentils for the synthesis of fluorescent carbon quantum dots and its application for sensing Fe3+, *Opt. Mater.*, 2019, **91**, 386–395.

84 L. Shi, G. Zhou, X. Xiang, Z. Zhang, Y. Jia, P. Liu and Z. Li, Nitrogen-sulfur co-doped pH-insensitive fluorescent carbon dots for high sensitive and selective hypochlorite detection, *Spectrochim. Acta, Part A*, 2020, **242**, 118721.

85 C. Wang, Y. Wang, H. Shi, Y. Yan, E. Liu, X. Hu and J. Fan, A strong blue fluorescent nanoprobe for highly sensitive and selective detection of mercury(II) based on sulfur doped carbon quantum dots, *Mater. Chem. Phys.*, 2019, **232**, 145–151.

86 T. Cai, H. Zhang, J. Chen, Z. Li and H. Qiu, Polyethyleneimine-functionalized carbon dots and their precursor co-immobilized on silica for hydrophilic interaction chromatography, *J. Chromatogr. A*, 2019, **1597**, 142–148.

87 X. Ren, C. Hu, D. Gao, Q. Fu, K. Zhang, F. Zu, J. Zeng, L. Wang and Z. Xia, Preparation of a poly(ethyleneimine) embedded phenyl stationary phase for mixed-mode liquid chromatography, *Anal. Chim. Acta*, 2018, **1042**, 165–173.

88 A. Gupta, A. Chaudhary, P. Mehta, C. Dwivedi, S. Khan, N. C. Verma and C. K. Nandi, Nitrogen-doped, thiol-functionalized carbon dots for ultrasensitive Hg(ii) detection, *Chem. Commun.*, 2015, **51**, 10750–10753.

89 X. Liu, N. Zhang, T. Bing and D. Shangguan, Carbon Dots Based Dual-Emission Silica Nanoparticles as a Ratiometric Nanosensor for Cu^{2+}, *Anal. Chem.*, 2014, **86**, 2289–2296.

90 H. Zhang, Y. Chen, M. Liang, L. Xu, S. Qi, H. Chen and X. Chen, Solid-Phase Synthesis of Highly Fluorescent Nitrogen-Doped Carbon Dots for Sensitive and Selective Probing Ferric Ions in Living Cells, *Anal. Chem.*, 2014, **86**, 9846–9852.

91 P. Shen and Y. Xia, Synthesis-Modification Integration: One-Step Fabrication of Boronic Acid Functionalized Carbon Dots for Fluorescent Blood Sugar Sensing, *Anal. Chem.*, 2014, **86**, 5323–5329.

92 A. Barati, M. Shamsipur and H. Abdollahi, Hemoglobin detection using carbon dots as a fluorescence probe, *Biosens. Bioelectron.*, 2015, **71**, 470–475.

93 H. Yuan, J. Yu, S. Feng and Y. Gong, Highly photoluminescent pH-independent nitrogen-doped carbon dots for sensitive and selective sensing of p-nitrophenol, *RSC Adv.*, 2016, **6**, 15192–15200.

94 H. K. Thabet, A. M. Ashmawy, M. A. Ali, E. A. El-Desouky and A. M. Abdel-Raoof, Analytical green star area (AGSA) as a new assessment tool for the electrochemical determination of cyclobenzaprine hydrochloride in wastewater samples using recycled graphite-modified nitrogen-doped CQDs, *RSC Adv.*, 2025, **15**, 34128–34137.

95 H. K. Thabet, A. M. Ashmawy, A. I. Hosameldin and A. M. Abdel-Raoof, Carbon quantum dots biomass waste-derived banana peel as a fluorescence probe for cyclobenzaprine hydrochloride determination in biological fluids and pharmaceuticals aided by green synthesis microwave-driven, *Microchem. J.*, 2025, **216**, 114700.

96 A. M. Abdel-Raoof, E. A. El-Desouky, A. M. Abdelzaher and R. H. Obaydo, Lemon zest-derived N,S-doped carbon quantum dots as a highly sensitive and sustainable fluorescent probe for cefoxitin sodium determination, *Talanta Open*, 2026, **13**, 100601.

97 M. B. Ali, A. M. Abdel-Raoof, H. M. Elbardisy, G. A. Omran, M. A. Ragab and S. Morshedy, Green "turn-off" luminescent nanosensor for the sensitive analysis of finerenone in various matrices: application of recent greenness assessment techniques, *RSC Adv.*, 2025, **15**, 46207–46217.

98 E. S. Permyakova, L. Yu. Antipina, A. M. Kovalskii, I. Y. Zhitnyak, K. Yu. Gudz, J. Polčak, P. B. Sorokin, A. M. Manakhov and D. V. Shtansky, Experimental and Theoretical Study of Doxorubicin Physicochemical Interaction with BN(O) Drug Delivery Nanocarriers, *J. Phys. Chem. C*, 2018, **122**, 26409–26418.

99 M. Z. Tonel, M. O. Martins, I. Zanella, R. B. Pontes and S. B. Fagan, A first-principles study of the interaction of doxorubicin with graphene, *Comput. Theor. Chem.*, 2017, **1115**, 270–275.

100 A. M. Sawy, A. Barhoum, S. A. Abdel Gaber, S. M. El-Hallouty, W. G. Shousha, A. A. Maarouf and A. S. G. Khalil, Insights of doxorubicin loaded graphene quantum dots: Synthesis, DFT drug interactions, and cytotoxicity, *Mater. Sci. Eng. C*, 2021, **122**, 111921.

101 C. Wang, L. Zhang, Y. Jiang, M. Zhang, L. Liu, D. Ye, S. Zhang and Y. Yang, A DFT study on the high-density assembly of doxorubicin drug delivery by single-walled carbon nanotubes, *Phys. E*, 2021, **134**, 114892.

102 L. Zhang, C. Wang, Y. Jiang, S. Zhang, D. Ye and L. Liu, Drug delivery mechanism of doxorubicin and camptothecin on single-walled carbon nanotubes by DFT study, *Appl. Surf. Sci.*, 2023, **614**, 156242.

103 R. Esfandiarpour, F. Badalkhani-Khamseh and N. L. Hadipour, Exploration of phosphorene as doxorubicin nanocarrier: An atomistic view from DFT calculations and MD simulations, *Colloids Surf., B*, 2022, **215**, 112513.

104 M. Perveen, L. Noreen, M. Waqas, R. F. Mehmood, J. Iqbal, S. Manzoor, S. Nazir, A. M. Shawky and R. A. Khera, A DFT approach for finding therapeutic potential of graphyne as a nanocarrier in the doxorubicin drug delivery to treat cancer, *J. Mol. Graph. Model.*, 2023, **124**, 108537.

105 H. Vovusha, D. Banerjee, M. K. Yadav, F. Perrozzi, L. Ottaviano, S. Sanyal and B. Sanyal, Binding Characteristics of Anticancer Drug Doxorubicin with Two-Dimensional Graphene and Graphene Oxide: Insights from Density Functional Theory Calculations and Fluorescence Spectroscopy, *J. Phys. Chem. C*, 2018, **122**, 21031–21038.

106 V. Nagarajan and R. Chandiramouli, Sorption studies and removal of chlortetracycline and oxytetracycline using theta phosphorene nanoribbon – A DFT outlook, *J. Mol. Liq.*, 2022, **346**, 117070.

107 L. Jing, W. Xuejiang, W. Yuan, X. Siqing and Z. Jianfu, Insight into the co-adsorption behaviors and interface interactions mechanism of chlortetracycline and lead onto struvite loaded diatomite, *J. Hazard. Mater.*, 2021, **405**, 124210.

108 S. Duan, Y. Gao, G. Lan, H. Qiu, B. Xu, X. Liu, M. Zhang and Y. Chen, Construction of ligand functionalized MIL-101(Fe)-R and mechanism of efficient removal of chlortetracycline hydrochloride: Experiment and DFT calculation, *Sep. Purif. Technol.*, 2024, **348**, 127753.

109 G. M. Khairy, S. M. Ragab, E. A. Moawed, R. R. El sadda and M. M. Aboelnga, Uncovering an effecient binary system as a chemosensor for visual and fluorescence detection of

chromium (VI) in water samples, *Spectrochim. Acta, Part A*, 2024, **321**, 124729.

110 A. M. Vervald, K. A. Laptinskiy, M. Yu. Khmeleva and T. A. Dolenko, Toward carbon dots from citric acid and ethylenediamine, part 1: Structure, optical properties, main luminophore at different stages of synthesis, *Carbon Trends*, 2025, **19**, 100452.

111 E. Elbayoumy, M. Elhendawy, M. M. Gaafar, E. A. Moawed and M. M. aboelnga, Novel fluorescent sensor based on triazole-pyridine derivative for selective detection of mercury (II) ions in different real water samples: Experimental and DFT calculations, *J. Mol. Liq.*, 2024, **401**, 124589.

112 E. Elbayoumy, M. O. Elassi, G. M. Khairy, E. A. Moawed and M. M. aboelnga, Development of efficient fluorescent sensor for the detection of hazard aromatic nitro compounds via N-(1-naphthyl)ethylenediamine: Experimental and DFT studies, *J. Mol. Liq.*, 2023, **391**, 123270.

113 E. Elbayoumy, M. Shaker, M. Gaafar, E. A. Moawed and M. M. Aboelnga, Eco-friendly one-step production of a highly sensitive fluorescent sensor for iron (III) detection in aqueous solutions: Experimental and DFT insights, *J. Photochem. Photobiol., A*, 2025, **466**, 116391.

114 M. J. Frisch, G. W. Trucks, H. B. Schlegel, G. E. Scuseria, M. A. Robb, J. R. Cheeseman, G. Scalmani, V. Barone, G. A. Petersson and H. Nakatsuji, *Gaussian 16, Revision a. 03*, Gaussian, Inc., Wallingford CT, 2016.

115 A. D. Becke, Density-functional thermochemistry. III. The role of exact exchange, *J. Chem. Phys.*, 1993, **98**, 5648–5652.

116 C. Lee, W. Yang and R. G. Parr, Development of the Colle-Salvetti correlation-energy formula into a functional of the electron density, *Phys. Rev. B*, 1988, **37**, 785–789.

117 S. H. Vosko, L. Wilk and M. Nusair, Accurate spin-dependent electron liquid correlation energies for local spin density calculations: a critical analysis, *Can. J. Phys.*, 1980, **58**, 1200–1211.

118 P. J. Stephens, F. J. Devlin, C. F. Chabalowski and M. J. Frisch, Ab Initio Calculation of Vibrational Absorption and Circular Dichroism Spectra Using Density Functional Force Fields, *J. Phys. Chem.*, 1994, **98**, 11623–11627.

119 J. S. Al-Otaibi, Y. S. Mary, Y. S. Mary, J. N. C. Mishma and A. Manikandan, Investigation of the adsorption and sensor properties of resorcinol (RSL) on X9N9 (X = Al, B, Ga, In) nanorings by DFT and QTAIM analysis with solvent effects, *J. Mol. Liq.*, 2024, **398**, 124285.

120 A. Kanzariya, S. Vadalkar, S. K. Jana, L. K. Saini and P. K. Jha, An ab-initio investigation of transition metal-doped graphene quantum dots for the adsorption of hazardous CO2, H2S, HCN, and CNCl molecules, *J. Phys. Chem. Solids*, 2024, **186**, 111799.

121 M. M. Aboelnga and S. Kalyaanamoorthy, QM/MM Investigation to Identify the Hallmarks of Superior PET Biodegradation Activity of PETase over Cutinase, *ACS Sustain. Chem. Eng.*, 2022, **10**, 15857–15868.

122 R. Kaur, M. M. Aboelnga, D. J. Nikkel and S. D. Wetmore, The metal dependence of single-metal mediated phosphodiester bond cleavage: a QM/MM study of a multifaceted human enzyme, *Phys. Chem. Chem. Phys.*, 2022, **24**, 29130–29140.

123 S. Lotfy, E. Elbayoumy, E. A. Moawed and M. M. Aboelnga, Atomistic insights into MgO nanoring as an efficient drug sensor for amphetamine derivatives, *J. Mol. Liq.*, 2025, **436**, 128256.

124 M. M. Aboelnga, M. M. Seliem, E. El-Bayoumy and M. El-Tahawy, DFT investigation of dye adsorption on pristine and doped graphdiyne: toward efficient removal of disperse yellow 3 from wastewater, *Nanoscale Adv.*, 2025, **7**, 7363–7381.

125 T. Lu and F. Chen, Multiwfn: A multifunctional wavefunction analyzer, *J. Comput. Chem.*, 2012, **33**, 580–592.

126 W. Humphrey, A. Dalke and K. Schulten, VMD: Visual molecular dynamics, *J. Mol. Graph.*, 1996, **14**, 33–38.

127 T. Williams, C. Kelley, H.-B. Bröker, J. Campbell, R. Cunningham, D. Denholm, G. Elber, R. Fearick, C. Grammes and L. Hart, *Gnuplot 4.6, an Interactive Plotting Program*, 2010.

128 A. Allouche, Gabedit—A graphical user interface for computational chemistry softwares, *J. Comput. Chem.*, 2011, **32**, 174–182.

129 S. K. Jana, D. Chodvadiya, N. N. Som and P. K. Jha, A quantum mechanical prediction of C24 fullerene as a DNA nucleobase biosensor, *Diam. Relat. Mater.*, 2022, **129**, 109305.

130 Md. A. Hossain, Md. R. Hossain, Md. K. Hossain, J. I. Khandaker, F. Ahmed, T. Ferdous and Md. A. Hossain, An ab initio study of the B35 boron nanocluster for application as atmospheric gas (NO,NO2,N2O,NH3) sensor, *Chem. Phys. Lett.*, 2020, **754**, 137701.

131 A. D. Allen and C. V. Senoff, INFRARED SPECTRA OF TRIS-ETHYLENEDIAMINE COMPLEXES OF RUTHENIUM (II), *Can. J. Chem.*, 1965, **43**, 888–895.

132 L. C. Bichara, H. E. Lanús, E. G. Ferrer, M. B. Gramajo and S. A. Brandán, Vibrational Study and Force Field of the Citric Acid Dimer Based on the SQM Methodology, *Adv. Phys. Chem.*, 2011, **2011**, 347072.

133 V. A. Ansi and N. K. Renuka, Exfoliated graphitic carbon dots: Application in heavy metal ion sensing, *J. Lumin.*, 2019, **205**, 467–474.

134 M. Margoshes and V. A. Fassel, The infrared spectra of aromatic compounds, *Spectrochim. Acta*, 1955, **7**, 14–24.

135 Y. Zhang, Y. Nie, R. Zhu, D. Han, H. Zhao and Z. Li, Nitrogen doped carbon dots for turn-off fluorescent detection of alkaline phosphatase activity based on inner filter effect, *Talanta*, 2019, **204**, 74–81.

136 B. Fang, X. Lu, J. Hu, G. Zhang, X. Zheng, L. He, J. Cao, J. Gu and F. Cao, pH controlled green luminescent carbon dots derived from benzoxazine monomers for the fluorescence turn-on and turn-off detection, *J. Colloid Interface Sci.*, 2019, **536**, 516–525.

137 J. Jia, B. Lin, Y. Gao, Y. Jiao, L. Li, C. Dong and S. Shuang, Highly luminescent N-doped carbon dots from black soya beans for free radical scavenging, Fe3+ sensing and cellular imaging, *Spectrochim. Acta, Part A*, 2019, **211**, 363–372.

138 S. R. Anand, A. Bhati, D. Saini, Gunture, N. Chauhan, P. Khare and S. K. Sonkar, Antibacterial Nitrogen-doped Carbon Dots as a Reversible "Fluorescent Nanoswitch" and Fluorescent Ink, *ACS Omega*, 2019, **4**, 1581–1591.

139 Z. Wang, D. Chen, B. Gu, B. Gao, T. Wang, Q. Guo and G. Wang, Biomass-derived nitrogen doped graphene quantum dots with color-tunable emission for sensing, fluorescence ink and multicolor cell imaging, *Spectrochim. Acta, Part A*, 2020, **227**, 117671.

140 K. Lawson-Wood, S. Upstone and K. Evans, Determination of Relative Fluorescence Quantum Yields using the FL6500 Fluorescence Spectrometer, *Fluoresc. Spectrosc.*, 2018, **4**, 1–5.

141 M. H. Gehlen, The centenary of the Stern-Volmer equation of fluorescence quenching: From the single line plot to the SV quenching map, *J. Photochem. Photobiol., C*, 2020, **42**, 100338.

142 T. Htun, A Negative Deviation from Stern–Volmer Equation in Fluorescence Quenching, *J. Fluoresc.*, 2004, **14**, 217–222.

143 X. Y. Sun, M. J. Yuan, B. Liu and J. S. Shen, Carbon dots as fluorescent probes for detection of VB_{12} based on the inner filter effect, *RSC Adv.*, 2018, **8**, 19786–19790.

144 J. Mo, S. Wang, J. Zeng and X. Ding, Aptamer-based Upconversion Fluorescence Sensor for Doxorubicin Detection, *J. Fluoresc.*, 2023, **33**, 1897–1905.

145 S. Swain, A. K. Jena and T. Mohanta, Ratiometric Fluorescence/Colorimetry/Smartphone Triple-Mode Real-Time Detection of Doxorubicin by Nitrogen-Doped Carbon Dots, *ACS Appl. Opt. Mater.*, 2023, **1**, 1236–1244.

146 J. Hu, R. Wang, R. Fan, Z. Huang, Y. Liu, G. Guo and H. Fu, Enhanced luminescence in Yb3+ doped core-shell upconversion nanoparticles for sensitive doxorubicin detection, *J. Lumin.*, 2020, **217**, 116812.

147 S. Xu, J. Ding and L. Chen, A fluorescent material for the detection of chlortetracycline based on molecularly imprinted silica–graphitic carbon nitride composite, *Anal. Bioanal. Chem.*, 2018, **410**, 7103–7112.

148 X. Cai, J. Ye, D. Duan and K. Li, Ratiometric fluorescence determination of chlortetracycline based on the aggregation of copper nanoclusters triggered by aluminum ion, *Microchim. Acta*, 2022, **189**, 28.

149 L. Yu, H. Chen, J. Yue, X. Chen, M. Sun, H. Tan, A. M. Asiri, K. A. Alamry, X. Wang and S. Wang, Metal–Organic Framework Enhances Aggregation-Induced Fluorescence of Chlortetracycline and the Application for Detection, *Anal. Chem.*, 2019, **91**, 5913–5921.

150 Y.-Q. Liang, X.-Y. Wu, J.-Y. Zeng, Y.-N. Wu, J.-P. Lai and H. Sun, A novel fluorescence ratio probe based on dual-emission carbon dots for highly selective and sensitive detection of chlortetracycline and cell imaging, *Anal. Bioanal. Chem.*, 2022, **414**, 3043–3055.